

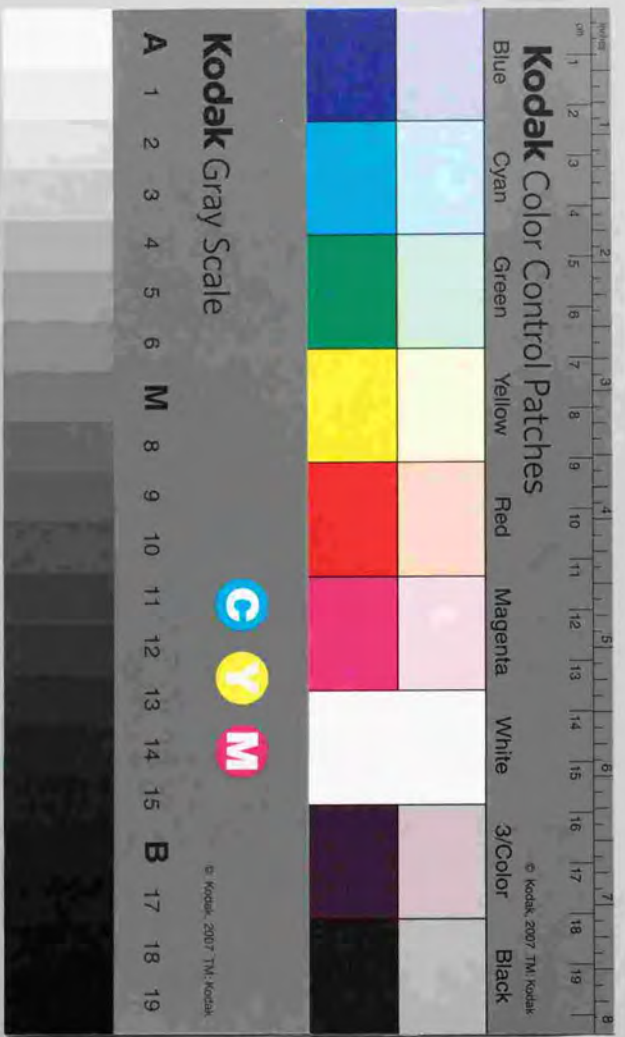
学位論文

First-principles studies of
chemical bonds and etching processes
at surfaces

表面化学結合とエッチングの
第一原理的研究

平成19年12月博士(理学)修了
東京大学大学院理学系研究科
物理科学専攻

相澤 勇太



0

Doctoral Thesis

First-principles studies of
chemical bonds and etching processes
at surfaces

Hideaki Aizawa

Institute for Solid State Physics
University of Tokyo

December 1997

Acknowledgements

I would like to express my sincere gratitude to Professor Shinji Tsuneyuki for his continual guidance and encouragement throughout the present work. Without his cordial support, this work could have never been achieved. I am grateful to him also for having introduced me to the fascinating fields of surface science and computational physics when I became a member of his group.

I am really happy to have been able to stay at the Institute for Solid State Physics (ISSP) for as long as five years, where there are/were so many distinguished surface scientists. I wish to express my appreciation to Prof. Y. Murata and Prof. K. Fukutani for having made me realize how attractive surface science is through their guidance when I was unfamiliar with it yet. I am grateful to Dr. T. Ogitsu for valuable discussions on semiconductor surfaces as well as his instructions on computer programming. I would like to thank Prof. K. Tanaka, Prof. F. Komori, Dr. K. Hattori, Dr. M.-B. Song and Dr. Y. Matsumoto for stimulating discussions on a wide range of interesting topics of surface science.

I would like to thank Dr. K. Kusakabe for fruitful discussions and kind advice. I wish to thank Prof. J.H. Weaver and Dr. K. Nakayama for valuable discussions on etching of semiconductor surfaces. I am grateful to Dr. T. Briere for her help in discussing the results of the population analysis for gaseous CO.

I would like to thank Prof. M. Tsukada, Prof. K. Tanaka, Prof. F. Komori, Prof. S. Hasegawa, and Prof. K. Fukutani for giving me valuable suggestions concerning this thesis.

The first-principles calculations in this work have been performed with a program which was originally coded by Dr. T. Ogitsu and has been improved by Dr. K. Kusakabe, Dr. Y. Tateyama, Dr. T. Miyake and Dr. T. Briere, who are all members of Prof. Tsuneyuki's group. The pseudopotentials used were from the database called NCPS95 produced by Dr. K. Kobayashi. I would like to thank all these people for allowing me to make use of those computational tools.

I would like to thank the Japan Society for the Promotion of Science for the fellowship.

I wish to thank Mrs. K. Fujii, Mrs. N. Sasaki and Mrs. M. Toda for encouraging me and giving me comfort when I was feeling low.

Last but not least, I would like to express my sincere thanks to my father for having advised me to be a researcher and my mother and sister for their continual encouragement throughout my life.

Contents

1	Introduction	1
2	Methods of calculation	7
2.1	Electronic structure calculations	7
2.1.1	Density functional theory and local density approximation	7
2.1.2	Ab-initio pseudopotentials and a plane wave basis set	10
2.1.3	Slab model vs. cluster model	14
2.2	Population analysis	17
2.2.1	Mulliken's analysis	17
2.2.2	Hoffmann's COOP curve	22
2.2.3	An analysis scheme applicable to wavefunctions expanded with a plane wave basis set	23
3	Chemisorption of CO on Pt(111):	
	Validity of the Blyholder Model	31
3.1	Introduction	31
3.2	Electronic structure of gaseous CO	35
3.3	Electronic structure of CO/Pt(111)	40
3.3.1	Computational conditions	40
3.3.2	Results and Discussions	42
3.4	Summary	53

4 Etching processes of Si(100) with adsorbed halogens and hydrogens	55
4.1 Introduction	55
4.2 Computational conditions	60
4.3 2×1 monohalide/monohydride surfaces	62
4.3.1 Surface structure	62
4.3.2 Desorption energy of adsorbates	64
4.4 3×1 surfaces	65
4.4.1 Surface structure	65
4.4.2 Stability of the 3×1 surface and estimation of the surface strain energy	68
4.4.3 Desorption energy of SiX ₂ units	69
4.5 Strain-free 2×1 surfaces with SiX ₂ units	73
4.6 Interpretation of experiments	75
4.7 Population analysis	79
4.8 H/Si(100) 1×1 surface	89
4.9 Summary	92
5 Concluding remarks	95
Appendix	99
References	103

Chapter 1

Introduction

Understandings of chemical bonds at surfaces are fundamental to investigations of surface chemical processes including those that are of technological importance such as catalytic reactions and surface etching. For example, a deeper understanding of bonds between alien molecules and a surface, i.e., chemisorption bonds, is expected to provide considerable insights into adsorption (sticking) and desorption processes, which are among the most important elementary processes composing surface chemical reactions. Also, it is essential for understanding, controlling and designing etching processes to clarify how adsorption of atoms or molecules affects chemical bonds between substrate atoms.

In this thesis, we investigate a few typical chemisorption systems ranging from metallic to semiconductor surfaces with emphases on properties of chemical bonds at surfaces. We employ the state-of-the-art first-principles calculational scheme based upon the density functional theory (DFT) [1, 2] combined with the local density approximation (LDA) [3], which has demonstrated its ability to reproduce and predict a variety of physical properties of a wide range of materials. A major part of recent DFT-LDA calculations for surfaces are characterized by the following two features: (1) A slab (or film) extended two-dimensionally infinitely is used to model a surface system rather than a small cluster. (2) A plane wave basis set is used to expand wavefunctions, in contrast to previous calculations in which wavefunctions

are usually described in the form of linear combinations of atomic orbitals (LCAO). Though the use of both a slab and a plane wave basis set greatly contributes to improved accuracies of calculations, at the same time it has been a major obstacle in fully understanding surface chemical bonds. This is originated in the fact that a chemical bond is a spatially local concept, whereas both a slab and a plane wave basis set are characterized by extended (delocalized) nature.

One of the main objectives of the present thesis is the development of a method of gaining a chemical view from such state-of-the-art calculations. Our chemical analysis scheme is in the spirit of that developed by Mulliken [4], which has been widely used in quantum chemical calculations for (isolated) molecules as well as small clusters to represent surface systems. In order to illustrate Mulliken's analysis briefly, let us consider the simplest case of the hydrogen molecule here. Suppose that a molecular orbital, ψ , is written in the form of a linear combination of the 1s atomic orbitals of each of the two hydrogen atoms (called the atoms 1 and 2 here), χ_1 and χ_2 , as

$$\psi = c_1\chi_1 + c_2\chi_2, \quad (1.1)$$

where χ_1 and χ_2 are assumed to be normalized. The orbital ψ should be normalized so that

$$\int |\psi|^2 d\tau = 1 = c_1^2 + c_2^2 + 2c_1c_2S_{12}, \quad (1.2)$$

where S_{12} is the overlap integral between χ_1 and χ_2 , which can be taken to be positive. The first (second) term in the right hand side of Eq. (1.2) can be considered to represent the number of electrons which belong to the atom 1(2) and is called the "net population" of the atom 1(2), while the third term corresponds to the number of electrons that can be assigned to the bonding region between the two atoms and is called the overlap population. A positive (negative) overlap population implies that the molecular orbital ψ has bonding (anti-bonding) character for the bond, as can be easily imagined from a simple molecular orbital theory which indicates that the (lowest-lying) bonding and anti-bonding orbitals of the hydrogen molecule are proportional

to $\chi_1 + \chi_2$ and $\chi_1 - \chi_2$, respectively. This idea is also applicable to a larger molecule to discuss how each of its molecular orbitals contributes to the specific bond of interest.

For such an extended system as represented by a slab, however, the population analysis becomes quite complicated, because such a system usually has as its eigenstates a great (or infinite in principle) number of spatially extended orbitals that contribute to the particular chemical bond of interest, with small contributions from each of those orbitals. Hoffmann et al. came up with the overlap population weighted density of states to be used for a simple analysis [5]. They call it the COOP curve, which is an abbreviation of the crystal orbital overlap population curve. Consider an orbital that is delocalized over L atoms, where L is large, but that still contributes to the chemical bond of interest. The overlap population with respect to the bond, that can be a measure of the contribution from this orbital to the bond, is then proportional to $1/L$, which is very small. The number of such orbitals, however, is proportional to L , so that the density of states weighted by such overlap populations assumes finite values. The COOP curve often provides a simple picture of a chemical bond in an extended system.

Our analysis scheme which will be described in the present thesis has a further advantage of being applicable to calculations in terms of plane wave basis sets. One of the major disadvantages involved in the use of plane wave basis sets is that one cannot readily extract chemical (and thus local) insights from wavefunctions expressed in terms of completely delocalized plane waves. This is at least one of the reasons why chemists still stick to LCAO-type calculations, for which well-established chemical analysis schemes such as Mulliken's population analysis and Hoffmann's COOP curve can be used straightforwardly. Now that calculations with plane wave basis sets have met with remarkable success, it is obvious that a chemical analysis scheme that is applicable to such calculations is in order.

In Chapter 2, we give a brief review of some of the methodologies upon which our first-principles electronic structure calculations are based, namely, the DFT-LDA scheme [1, 2, 3], the ab initio pseudopotential technique com-

bined with the plane wave basis set [6], and the slab model to represent a surface system. The DFT-LDA scheme has been quite successful in quantitatively reproducing and predicting various properties of a variety of systems. Furthermore, it helps reduce computational costs greatly as compared to conventional quantum chemical calculational schemes such as the Hartree-Fock method. In the pseudopotential technique, the nucleus and core electrons of each atom in the system are replaced by a pseudopotential and only the valence electrons are explicitly treated. Calculations with pseudopotentials are advantageous over all-electron calculations (in which the core electrons are also explicitly treated) for several reasons that will be described later. One of the reasons is that the use of pseudopotentials allows expansions of one-electron wavefunctions with a moderate number of plane waves [7], thus enabling the use of the plane wave basis set. By using it, one can readily improve the accuracy of an electronic structure calculation in contrast to the LCAO-type basis sets. The slab model is superior to the cluster model not just because the former represents the surface more realistically than the latter but also because the former allows a fast convergence of calculated quantities with respect to the number of layers in the slab. In this chapter we will also explain in more details the conventional population analysis schemes described briefly above. Finally, a newly-developed analysis scheme applicable to calculations with plane wave basis sets will be described [8].

In Chapter 3, we discuss the mechanism of the bonding of CO to Pt(111) surface [8]. CO molecules chemisorbed on transition metal surfaces are among the most extensively studied systems in surface science, partly because they often exhibit catalytic reactivities. The bonding of CO to transition metal surfaces has been understood in terms of the Blyholder model [9], which is in the spirit of the frontier orbital theory in that only the HOMO and LUMO of the molecule, namely the 5σ and 2π orbitals, are involved in the bonding. In this model the bonding is considered to be derived from two contributions: the 5σ donation and 2π backdonation. These are the effects of the interaction of the corresponding molecular orbitals with the metal bands, where the 5σ orbital, which is completely filled in the gas phase, becomes

partially empty, while the originally empty 2π orbitals become partially filled. Although the Blyholder model has been widely accepted because of its simple and lucid way of describing the bonding mechanism, several studies, both experimentally [10, 11, 12] and theoretically [13, 14], pointed out deficiencies of the model. For instance, a semi-empirical extended Hückel calculation for CO/Pt(111) suggested that the 4σ orbital could also contribute to the bonding [13]. Recently, X-ray emission spectroscopy (XES) studies for CO/Ni(111) by Nilsson et al. indicated the existence of states localized on one of the atoms composing CO, and they argued that an atomic-orbital-based picture is needed to describe the bonding of CO to the surface rather than a molecular-orbital-based one like the Blyholder model. We reexamine the adequacy of the Blyholder model by means of the state-of-the-art first-principles calculations combined with the new population analysis scheme introduced in Chap. 2. As a result of the population analysis, the 4σ and 1π orbitals of CO are found to be completely filled, showing that they do not play a role in the bonding of CO to the surface. On the other hand, the calculated populations of the 5σ and 2π orbitals indicate that there are substantial 5σ donation and 2π backdonation. These results definitely show that the Blyholder model allows an accurate and at the same time simple description of the chemisorption mechanism, in spite of the fact that a part of the one-electron states are localized on one of the atoms of CO as a result of rehybridization of some of the molecular orbitals of CO upon adsorption.

In Chapter 4, we study the X/Si(100) surfaces with X representing H, Cl, Br or I. An emphasis is laid on the strength of the Si-Si backbonds in the presence of the different adsorbates, since their cleavages result in etching of the Si substrate, which plays an essential role in the device manufacturing technology. In fact, some of these surfaces have been reported to be susceptible to etching. Thermal desorption studies for Cl/Si(100) [15, 16, 17] and Br/Si(100) [18, 19] showed that the dihalide species (SiCl_2 and SiBr_2) were among the main products. In contrast, it was shown that for H/Si(100) almost all the adsorbed hydrogens are thermally desorbed as H_2 molecules and desorption of silicon hydride species was rarely observed [20, 21]. For

I/Si(100), etching does not proceed efficiently either, the main products being I atoms [18]. We address the question as to why such etching processes (i.e., desorption of silicon-containing compounds) are promoted by the adsorption of Cl and Br but not by that of H and I by means of the DFT-LDA electronic structure calculation and the population analysis scheme described in Chap. 2. We consider two kinds of surfaces involving SiX₂ species on them, both of which can be intermediate states of the etching process. Based on the calculated desorption energies of the SiX₂ units for each type of the surfaces, we argue that they are determined by two factors, namely, a weakening of the backbonds induced by the presence of the adsorbates and destabilization of the surface structure due to the interatomic repulsions between the adsorbates. It is shown that such a picture can consistently explain the available thermal desorption data. The population analysis indicates that the bond charge of the backbonds is reduced significantly by the presence of some of the adsorbates under consideration, which can be considered to be responsible for the weakening of the backbonds.

In Chapter 5, concluding remarks are given.

Chapter 2

Methods of calculation

2.1 Electronic structure calculations

2.1.1 Density functional theory and local density approximation

Many of quantum chemical calculations including those for small clusters modeling surface systems have been based upon the Hartree-Fock (HF) approximations [22]. As the HF equation involves the complicated non-local exchange term in addition to the local electrostatic (Hartree) term, the equation is an integrodifferential equation that is difficult to solve. For example, if the one-electron wavefunctions are expanded by N atomic orbitals following the conventional LCAO (Linear Combination of Atomic Orbitals) approach, then the number of matrix elements that should be calculated and stored in the memory of a computer is proportional to N^4 , which makes calculations for large molecules and solids difficult. There are other quantum chemical approaches that are more refined than the HF method in the sense that effects of electron correlations, which are completely neglected in the HF method, are included to some extent such as the CI method [23]. They usually require even more calculational costs than the HF method, making their applications to large molecules and solids completely prohibitive. Although Slater proposed a way of replacing the non-local exchange term in the HF equation

with a local one, known as the $X\alpha$ method [22], it involves an adjustable parameter α and is of semi-empirical nature.

The density functional theory (DFT) [1, 2] combined with the local density approximation (LDA) [3] resolves the above-mentioned difficulty concerning computational costs. The DFT is a theory for many-electron systems and is based on the Hohenberg-Kohn theorem [1]. The theorem states that all one has to do in order to obtain the total energy and electron density distribution of the ground state of a system of N electrons moving in a given external potential $v_{\text{ext}}(\mathbf{r})$ (typically consisting of the interactions between electrons and nuclei) is to minimize the following functional $E[n(\mathbf{r})]$ of the electron density distribution function $n(\mathbf{r})$ (in atomic units):

$$E[n(\mathbf{r})] = T_s[n(\mathbf{r})] + \frac{1}{2} \int \frac{n(\mathbf{r})n(\mathbf{r}')}{|\mathbf{r} - \mathbf{r}'|} d\mathbf{r}d\mathbf{r}' + E_{\text{xc}}[n(\mathbf{r})] + \int n(\mathbf{r})v_{\text{ext}}(\mathbf{r})d\mathbf{r}. \quad (2.1)$$

Here $T_s[n]$ and $E_{\text{xc}}[n]$ represent kinetic and exchange-correlation energies, respectively. Of course, the minimization should be subject to the condition

$$\int n(\mathbf{r})d\mathbf{r} = N. \quad (2.2)$$

The minimal value of $E[n(\mathbf{r})]$ and the function $n(\mathbf{r})$ that minimizes $E[n(\mathbf{r})]$ are the total energy and the electron density distribution of the *ground state*, respectively. Such a minimization procedure was shown by Kohn and Sham [3] to be equivalent to self-consistently solving the following set of equations for one electron wavefunctions $\{\psi_i(\mathbf{r})\}$:

$$-\frac{1}{2}\nabla^2 + v_{\text{eff}}(\mathbf{r})\psi_i(\mathbf{r}) = \epsilon_i\psi_i(\mathbf{r}), \quad (2.3)$$

where the effective potential $v_{\text{eff}}(\mathbf{r})$ is given by

$$v_{\text{eff}}(\mathbf{r}) = v_{\text{ext}}(\mathbf{r}) + \int \frac{n(\mathbf{r}')}{|\mathbf{r} - \mathbf{r}'|} d\mathbf{r}' + v_{\text{xc}}(\mathbf{r}), \quad (2.4)$$

and

$$n(\mathbf{r}) = \sum_i^{\text{occ.}} |\psi_i(\mathbf{r})|^2 \quad (2.5)$$

with the sum carried out over the N lowest (occupied) eigenstates. $v_{\text{xc}}(\mathbf{r})$ is defined by

$$v_{\text{xc}}(\mathbf{r}) = \frac{\delta E_{\text{xc}}[n(\mathbf{r})]}{\delta n(\mathbf{r})}. \quad (2.6)$$

The exact form for $E_{\text{xc}}[n(\mathbf{r})]$ (and thus $v_{\text{xc}}(\mathbf{r})$) is unknown, reflecting the fact that the exact solutions for ground state properties of many electron systems cannot be obtained in practice. If $n(\mathbf{r})$ is sufficiently slowly varying with \mathbf{r} , however, one gets a simple expression

$$E_{\text{xc}}[n(\mathbf{r})] = \int n(\mathbf{r})\epsilon_{\text{xc}}(n(\mathbf{r}))d\mathbf{r} \quad (2.7)$$

as a first approximation, where $\epsilon_{\text{xc}}(n)$ represents the exchange correlation energy per electron of a *uniform* electron gas with density n [3]. Such an approximation is called the LDA. The LDA has been shown to give surprisingly good results for a variety of properties of a wide range of materials [2].

Calculations with the DFT-LDA scheme are superior to those with the Hartree-Fock approximation (HFA) in the following two respects:

1. The equation (2.3), which is often called the Kohn-Sham equation, is much simpler to solve than the Hartree-Fock equation, since the former does not include such a complicated term as the non-local exchange term in the latter. (Note that the Kohn-Sham equation involves semi-local terms as pseudopotentials in some cases, but computer time and storage required can be greatly reduced by transforming them into *separable* non-local forms as described below.) Computational costs are much smaller with the LDA than with the HFA, thus making calculations for large molecules and solids possible.
2. The LDA incorporates effects of electron correlations to some extent (in v_{xc}), which are completely omitted in the HFA, and is therefore expected to yield more accurate results than the HFA, as it actually does.

The DFT-LDA scheme is especially preferred in surface calculations, where the use of larger unit cells is required than in bulk calculations. In Appendix

A, a review of the development of the DFT-LDA approach to surfaces is given.

Finally, we should comment on v_i and ϵ_i in Eq. (2.3). Formally, they have been introduced as auxiliary quantities to simplify the minimization procedure of $E[n(\mathbf{r})]$ in Eq. (2.1) and do not have any justified physical meanings, though discussions in terms of them have been actually performed frequently. In order to get quasiparticle energies $\tilde{\epsilon}_i$ (corresponding to ionization energies) and quasiparticle wavefunctions $\tilde{\psi}_i$ that have physical meanings, one has to solve the following quasiparticle equation (called Hedin's equation):

$$-\frac{1}{2}\nabla^2\tilde{\psi}_i(\mathbf{r}) + \int \Sigma(\mathbf{r}, \mathbf{r}'; \tilde{\epsilon}_i)\tilde{\psi}_i(\mathbf{r}')d\mathbf{r}' = \tilde{\epsilon}_i\tilde{\psi}_i(\mathbf{r}), \quad (2.8)$$

where Σ is a non-local, non-Hermitian and energy-dependent self energy operator [24, 25]. By expanding Σ as a series of the screened interaction W and taking account of only the first term GW (the so-called GW approximation), where G is the Green's function, one can solve the above complicated equation, though a huge amount of computations are still required. Hybertsen and Louie performed such calculations for several covalent and ionic solids, and found that the wavefunctions obtained from the Kohn-Sham equation are almost identical to those from the quasiparticle equation [26]. They also showed that there are significant differences between eigenvalues obtained with these two equations for some of the materials they studied. However, it has been well known that Kohn-Sham eigenvalues reproduce band structures of various materials at least qualitatively. Therefore analyses of Kohn-Sham wavefunctions and eigenvalues are expected to yield important information irrespective of the fact that there have been no proofs that justify their physical meanings as yet.

2.1.2 Ab-initio pseudopotentials and a plane wave basis set

The reasons why calculations with pseudopotentials are preferred rather than all-electron calculations are as follows: (1) Computational costs are

reduced by neglecting core electrons. (2) Since core electrons have much larger binding energies than valence electrons, the total energy of a system usually exhibits a very large negative value in all-electron calculations. Since the energy difference between two given atomic configurations is very small compared to the total energy, numerical errors might arise in determining, e.g., the equilibrium atomic structure. Due to the neglect of core electrons in pseudopotential calculations, the absolute value of the total energy is greatly reduced, and a high accuracy can be achieved in discussing the total energy as a function of atomic positions [27]. (3) Pseudopotentials allow the use of a plane wave basis set instead of an LCAO-type basis set, since they make possible the expansions of one-electron wavefunctions in terms of a moderate number of plane waves [7]. With a plane wave basis set, a wavefunction with its crystal momentum \mathbf{k} , $\psi_{\mathbf{k}}(\mathbf{r})$, is expressed as

$$\psi_{\mathbf{k}}(\mathbf{r}) = \sum_{\mathbf{G}} c_{\mathbf{k}+\mathbf{G}} e^{i(\mathbf{k}+\mathbf{G})\cdot\mathbf{r}}, \quad (2.9)$$

where only plane waves whose energy, $(k+G)^2/2$, is smaller than a certain cutoff value are included as basis functions. Some advantages involved in the use of a plane wave basis set are described in the following.

There are various kinds of LCAO-type basis sets (such as minimal, DZ (double zeta), DZ+P (polarization), ...), and results of LCAO-type calculations often depend critically upon which basis set is used. The use of a plane wave basis set allows one to overcome the difficulty of the basis-set dependence encountered in LCAO-type calculations, since a plane wave basis set has only one parameter, that is, the energy cutoff of plane waves and one can systematically improve the accuracy of a calculation just by increasing the energy cutoff. All one has to check regarding the basis set in order to ensure that a calculation is reliable is the convergence of calculated quantities with respect to the energy cutoff. The use of a plane wave basis set is preferred also because it simplifies calculations of the Hellmann-Feynman forces acted upon each atom in the system, which are needed in geometrical optimization procedures as well as ab initio molecular dynamics simulations [6]. This is due to the fact that plane wave basis states do not depend upon the po-

sition of atoms, which is not the case in calculations where wavefunctions are expressed in the form of linear combinations of atomic orbitals or their variants, that is, basis functions centered on each atom in the system.

However, a plane wave basis set has a disadvantage concerning computational costs, that is, a large number of plane waves are usually required to accurately describe (pseudo)wavefunctions. Especially, in calculations for surfaces where a real semi-infinite surface is approximated with periodically repeated slabs separated by a vacuum region, the size of the unit cell (called "super-cell") is usually large in the surface normal direction, resulting in an even larger number of plane waves. This is why a plane wave basis set had not been used until the mid-1980's. Such difficulties were largely mitigated by the progress of computer power along with the development of efficient calculational schemes [6] such as the Car-Parrinello algorithm [28] and the conjugate gradient technique [29]. These schemes enable one to solve the KS equation much more efficiently than the conventional matrix diagonalization scheme. Furthermore, Kleinman and Bylander proposed a scheme of transforming a semi-local pseudopotential into a non-local separable form which leads to a significant reduction in computational costs [30]. Also, Troullier and Martins (TM) [31] proposed soft pseudopotentials with which the number of plane waves required can be greatly reduced (especially for first-row elements and transition metal ones) compared with the conventional Hamann-Schlüter-Chiang [32] and Bachlet-Hamann-Schlüter (BHS) [33] pseudopotentials that had been widely used. Ultrasoft pseudopotentials without the norm-conserving condition that allow the use of an even smaller-sized plane wave basis set were also proposed by Vanderbilt [34]. Thus computational workload required for calculations with pseudopotentials and a plane wave basis set is now becoming smaller and smaller, making them more and more commonly used except when one is interested in phenomena in which core electrons play a crucial role as in X-ray photoemission.

Our calculations adopted ab initio norm-conserving pseudopotentials in the Kleinman-Bylander separable form. Those for some elements were of the BHS-type, while those for the others were generated following the Troullier-

Martins procedures. These pseudopotential techniques are described in more details in the following.

Ab initio norm-conserving pseudopotentials V_{PS} (corresponding to v_{ext} in Eq. (2.4)) such as those of the BHS [33] and TM [31] types are in general written as

$$V_{PS}(\mathbf{r}) = V_L(r) + \sum_{lm} |Y_{lm}(\theta, \phi)\rangle \delta V_l(r) \langle Y_{lm}(\theta, \phi)|, \quad (2.10)$$

where $|Y_{lm}(\theta, \phi)\rangle$ represents the spherical harmonics and the local potential V_L can be arbitrarily chosen. The second term in the right hand side of Eq. (2.10) implies that only the l -angular-momentum components of the wavefunctions are subject to δV_l . Therefore $V_l (\equiv V_L + \delta V_l)$ acts on them in total. V_l is constructed so that the radial part of the atomic (pseudo)wavefunction, $\varphi_l(r)$, which is obtained from the atomic calculation with V_l , satisfies the following requirements:

1. It should be nodeless.
2. It should, when normalized, be identical to the true wavefunction (i.e. the wavefunction obtained from the ab initio all-electron calculation) for $r > r_c$, where r_c is some cutoff radius.

One can obtain V_l that has such a pseudo-wavefunction as one of its eigenfunctions with the true eigenenergy just by inverting the radial Schrödinger equation. The first requirement above is imposed in order to make the pseudo-wavefunction smooth enough to allow its expansion with a moderate number of plane waves as well as to make the inversion of the radial Schrödinger equation feasible. The second requirement guarantees that the integrated charge, $4\pi \int_0^r \{\varphi_l(r')\}^2 r'^2 dr'$, is identical to the true value for $r > r_c$. This is important not only because the pseudopotential produces the correct electrostatic (Hartree) potential outside the sphere of radius r_c , but also because the correct integrated charge leads to an improved transferability of the pseudopotential, which can be seen from the following identity:

$$-2\pi \{(r'\varphi_l(r'))^2 \frac{d}{d\epsilon} \frac{d}{dr} \ln \varphi_l(r')\}_{r=r} = 4\pi \int_0^r \{\varphi_l(r')\}^2 r'^2 dr' \quad (2.11)$$

Since the radial logarithmic derivative of φ_l is directly related to the scattering phase shift, the identity with the correct integrated charge implies that the scattering properties of the pseudopotential and the true potential have the same energy variation to first order when transferred to other systems such as molecules and solids whose eigenenergies are different from those for the atom. There are an infinite number of pseudo-wavefunctions that satisfy the above two requirements, since there remains arbitrariness in choosing the form of the pseudo-wavefunction for $r < r_c$. By taking advantage of such arbitrariness, Troullier and Martins proposed a scheme of constructing pseudo-wavefunctions that lead to soft (i.e., smooth) pseudopotentials which require a smaller number of plane waves in the expansions of wavefunctions than conventional schemes [31].

As displayed in Eq. (2.10), a pseudopotential generally has a semi-local (i.e., local in the radial coordinate and nonlocal in the angular coordinates) term, which greatly increases the number of matrix elements that should be calculated. Kleinman and Bylander (KB) have overcome this difficulty by devising a separable form of a pseudopotential

$$V_{KB}(\mathbf{r}) = V_L(r) + \sum_{lm} \frac{|\delta V_l(r)\Phi_{lm}(\mathbf{r})\rangle\langle\Phi_{lm}(\mathbf{r})\delta V_l(r)|}{\langle\Phi_{lm}(\mathbf{r})|\delta V_l(r)|\Phi_{lm}(\mathbf{r})\rangle}, \quad (2.12)$$

where $\Phi_{lm}(\mathbf{r})(\equiv \varphi_l(r)Y_{lm}(\theta, \phi))$ is the whole pseudo-wavefunction [30]. V_{KB} and V_{PS} in Eq. (2.10) can be shown to be completely equivalent for the atomic calculation, and the replacement of V_{PS} with V_{KB} is expected to be valid in other situations such as molecules and solids as well by suitably choosing $V_L(r)$. The use of such separable pseudopotentials has now become very common, since it achieves substantial savings in the amount of computations as well as memory requirements.

2.1.3 Slab model vs. cluster model

The cluster model, which has been commonly used to investigate adsorption systems, is based on the "surface molecule" picture [35]. This picture assumes that a cluster ("surface molecule") composed of the adsorbate and

M	E_{ad} [kJ/mol]
1	57
2	83
3	90
4	95
5	99

Table 2.1: The calculated adsorption energies, E_{ad} , of CO on Cu slabs modeling Cu(100) that consist of M metal layers. The calculations were based on the DFT-LDA scheme. After Ref. [36].

one or a few substrate atoms around it can describe well the chemisorption bond. Such an approach is advantageous because a lot of calculational techniques in the field of quantum chemistry that are well-established for small (isolated) molecules can be straightforwardly applied. Thus numerous calculations using small clusters to represent adsorption systems have been performed thus far.

However, it should be always realized that the "surface molecule" picture is not always valid, though it often serves as a good starting point. In a more realistic surface calculation, a slab (or a film) which has finite width but is two-dimensionally extended is used to represent the surface. The use of a slab has been made possible by the development of the DFT-LDA scheme, which is computationally much less demanding than the HF method, as described in Subsec. 2.1.1. The advantage of the use of a slab over the use of a cluster is that the former represents more accurately a real surface that is laterally infinite. While most substrate atoms have a wrong coordination in a cluster, all atoms at the surface of a slab have a correct coordination. Besides, there is another reason why the slab model is preferable to the cluster model. *te Velde* recently reported the dependence of the adsorption energy of CO on Cu(100) upon the number of layers in the slab [36]. The result for the on-top species with a coverage of 1 ML is shown in Table 2.1. Although the result for $M = 1$ (corresponding to the calculation for CO on a Cu monolayer

N	E_{ad} [kJ/mol]
1	95
5	97
9	125
9(5+4)	65
21	109
30(13+12+5)	183
37	60

Table 2.2: The calculated adsorption energies, E_{ad} , of CO on Cu clusters modeling Cu(100) that consist of N metal atoms. For the clusters composed of two or more metal layers, the numbers of the atoms in each layer are also given in parentheses. The calculations were based on the DFT-LDA scheme. After Ref. [36].

film) is quite different from the results for M larger than 1, it can be seen that 3 (or even 2) layers suffice to give a reasonably converged result. The convergence with respect to the number of layers is important when one needs a result for the real semi-infinite surface, and the slab model allows a relatively fast convergence with respect to the number of layers, which is a great advantage over the cluster model. The dependence of the adsorption energy of CO on Cu(100) upon the number of atoms in the cluster model is shown in Table 2.2 [36]. In contrast to the case of the slab calculations, the adsorption energy does not exhibit a convergent behavior as the size of the cluster increases. Thus one can never expect how large the adsorption energy is at the real semi-infinite surface. The calculations mentioned above were performed with the DFT-LDA scheme, while HF cluster calculations for CO/Cu(100) yielded even worse results, which are presented in Table 2.3 [37]. The calculations for some of the clusters yielded negative adsorption energies, implying that CO does not adsorb on Cu(100) in contradiction to experiments. The failure of the clusters to properly represent the real surface can be at least partly attributed to their artificially large surface areas.

N	E_{ad} [kJ/mol]
1	-53
5	43
10	-39
14	27
34	-53

Table 2.3: The calculated adsorption energies, E_{ad} , of CO on Cu clusters modeling Cu(100) that consist of N metal atoms. The calculations were based on the Hartree-Fock approximation. After Ref. [37].

2.2 Population analysis

2.2.1 Mulliken's analysis

One of the most powerful methods for chemical analysis is Mulliken's population analysis [4], which has been commonly used in the field of quantum chemistry and is straightforwardly applicable to cluster calculations for investigating adsorption systems. Mulliken proposed in his original paper [4] several quantities which are quite helpful in obtaining chemical views of bonding in small molecules. The (total) *gross population* is a quantity that represents the number of electrons that are assigned to a particular atom (or atomic orbital) in the molecule, thus indicating how the atom is charged (or how many electrons are populated in the atomic orbital). The (total) *overlap population* with respect to a particular bond in the molecule serves as a measure of the strength of the bond. Since this quantity can be decomposed into the contributions from each molecular orbital (called the partial overlap populations), we can gain insight into which orbitals contribute much to the bonding. If the contribution from an orbital has a positive value, then populating electrons in it leads to a strengthening of the bond (bonding contribution), while if the contribution has a negative value, populating electrons in it results in a weakening of the bond (anti-bonding contribution).

We have described Mulliken's population analysis briefly in Chap. 1 for the simplest case of a hydrogen molecule. Let us generalize the description to the case of a larger molecule (or cluster). Suppose that each of its molecular orbitals (MO's) $\{\psi_\mu\}$ is expressed in the form of a linear combination of atomic-orbital-like basis functions $\{\chi_r\}$ as

$$\psi_\mu = \sum_r c_r^\mu \chi_r, \quad (2.13)$$

where each member of $\{\chi_r\}$ is centered on one of the atoms in the molecule. The normalization condition requires that

$$\int |\psi_\mu|^2 d\tau = 1 = \sum_r |c_r^\mu|^2 + \sum_{r \neq s} (c_r^\mu)^* c_s^\mu S_{rs}, \quad (2.14)$$

where S_{rs} is the overlap integral between χ_r and χ_s . The overlap term $(c_r^\mu)^* c_s^\mu S_{rs}$ is denoted by p_{rs}^μ hereafter. The definitions of several kinds of populations are given below.

The *partial overlap population*, p_{X-Y}^μ , with respect to the bond between two atoms of interest, say the atoms X and Y, is defined by the sum of the overlap terms p_{rs}^μ over the basis functions centered on the atom X and those on the atom Y, i.e.,

$$p_{X-Y}^\mu = \sum_{r \in \tilde{X}} \sum_{s \in \tilde{Y}} \{p_{rs}^\mu + (p_{rs}^\mu)^*\}, \quad (2.15)$$

where \tilde{X} and \tilde{Y} are the sets of the basis functions centered on the atoms X and Y, respectively. p_{X-Y}^μ indicates the contribution from the MO ψ_μ to the bonding between the atoms X and Y, with a positive (negative) value corresponding to a bonding (anti-bonding) contribution. The *total overlap population* for the X-Y bond, p_{X-Y} , is defined by the sum of the partial overlap populations over all the occupied orbitals, that is,

$$p_{X-Y} = \sum_\mu n_\mu p_{X-Y}^\mu. \quad (2.16)$$

Here n_μ is the occupation number of the one-electron state ψ_μ , which is 2 (including both spin states) for occupied states and 0 for unoccupied states.

This quantity serves as a rough measure of the bond strength, and is sometimes called the *bond charge*.

The *partial gross population*, q_X^μ , of a particular atom, say the atom X, is defined by

$$q_X^\mu = \sum_{r \in \tilde{X}} |c_r^\mu|^2 + \frac{1}{2} \sum_{r \in \tilde{X}} \sum_{s \notin \tilde{X}} \{p_{rs}^\mu + (p_{rs}^\mu)^*\}. \quad (2.17)$$

The first term of the right hand side of Eq. (2.17) is called the net population of the atom X, but will not be used in the present thesis. The coefficient $\frac{1}{2}$ of the second term implies that a half of the overlap population for the bond between the atoms X and Y, for instance, is taken to belong to the atom X and the other half to the atom Y. The *total gross population* of the atom X, q_X , is then given by

$$q_X = \sum_\mu n_\mu q_X^\mu. \quad (2.18)$$

Since the sum of the total gross populations over all the atoms is equal to the total number of electrons in the molecule, the total gross population of the atom X can be interpreted as the number of electrons assigned to the atom X. This quantity is also called the *Mulliken charge* (of the atom X).

In order to illustrate the usefulness of the above analysis scheme, we describe a study on photo-induced desorption of CO from a Pt surface [38, 39] in the following. Figure 2.1 displays the overlap population for the Pt-C bond in a three-atom cluster composed of Pt, C and O atoms modeling a CO/Pt system calculated within the Hartree-Fock approximation [39]. It can be seen that the occupied molecular orbitals designated as "4 σ ", "5 σ " and "1 π " as well as some of the Pt-derived orbitals are shown to give bonding contributions to the bond in the ground state. (This does not necessarily imply that the corresponding molecular orbitals of a *free* CO molecule such as the 4 σ and 1 π play a role in the formation of the chemisorption bond, as will be discussed in the next chapter.) It is also apparent that the unoccupied orbitals designated as "2 π^* " (doubly degenerate) and "Pt *sp* σ " have anti-bonding characters, the latter being much more anti-bonding than the former. By performing configuration interaction (CI) calculations that are

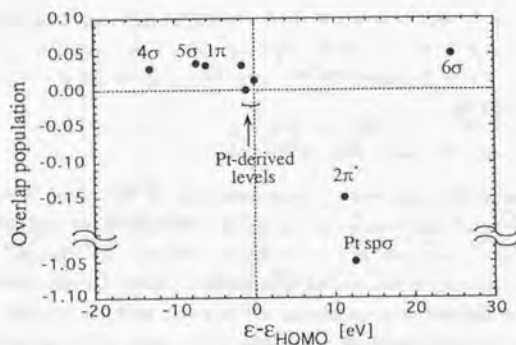


Figure 2.1: The overlap populations with respect to the Pt-C bond for each orbital of the three-atom PtCO cluster. Positive and negative values indicate bonding and antibonding contributions, respectively.

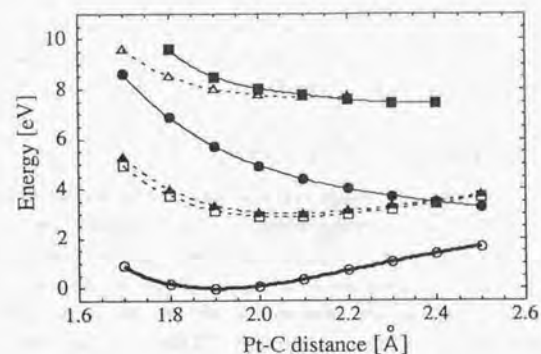


Figure 2.2: The potential energy surfaces as functions of the distance between Pt and C in the three-atom PtCO cluster calculated with the configuration interaction method.

valid for (electronically) excited states as well as the ground state, potential energy surfaces (PES) were obtained as functions of the distance between Pt and C. For simple discussions, we show in Fig. 2.2 the PES's calculated with a minimal basis set. For more quantitative results obtained with a larger basis set, see Ref. [38] and [39]. The bold line in Fig. 2.2 represents the ground state PES, while the solid and dashed lines correspond to excited states with an electron excited to the Pt $sp\sigma$ and $2\pi^*$ levels, respectively. As expected from Fig. 2.1, electronic transitions to the Pt $sp\sigma$ level, which exhibits large anti-bonding character, lead to repulsive PES's. Electronic transitions to the $2\pi^*$ levels, which have much less anti-bonding character than the Pt $sp\sigma$ level, do not result in repulsive PES's, though they lead to PES's with their minimum points located slightly farther from the surface compared to that of the ground state PES. This reflects the small negative value for the overlap population of the $2\pi^*$ levels. This example illustrates that by calculating the

overlap populations with respect to the particular bond of interest one can gain insight into not only the question as to why the bond can stably exist in the ground state but also the question as to how it can be made unstable, leading to desorption, dissociation, etching and so on.

2.2.2 Hoffmann's COOP curve

In calculations for extended systems such as slabs that model surfaces, it is not easy to achieve a simple understanding of a specific bond of interest, since it is often the case that there are a numerous number of orbitals relevant to it. As described in Chap. 1, Hoffmann et al. proposed the overlap population weighted density of states to overcome such a difficulty, which they call the crystal orbital overlap population curve, or the COOP curve for short. The COOP curve with respect to the bond between, say, the atoms X and Y, $N_{X-Y}(\epsilon)$, is given by

$$N_{X-Y}(\epsilon) = \sum_{\mu} p_{X-Y}^{\mu} \delta(\epsilon - \epsilon_{\mu}), \quad (2.19)$$

where μ is the index representing each one-electron state (with its energy ϵ_{μ}) of the system.

Hoffmann et al. studied several chemisorption systems with this analysis scheme. Figure 2.3 shows the COOP curve for the CO/Ni(100) $c(2 \times 2)$ chemisorption system calculated by his group [40]. The solid and dotted lines represent the COOP curve with respect to the Ni-C and C-O bonds, respectively. It can be clearly seen that the states just below the Fermi level (ϵ_f) give anti-bonding contributions to the C-O bond, from which one can guess that most of them are derived from the CO $2\pi^*$ levels. They give, on the other hand, bonding contributions to the Ni-C bond, which clearly indicates that these $2\pi^*$ -derived states play a role in the formation of the chemisorption bond. (Such an effect is called the 2π backdonation, as will be explained in more details in the next chapter.) From this example one can see that a COOP curve is a very convenient tool for gaining insights into chemical bonds in extended surface systems.

2.2. Population analysis

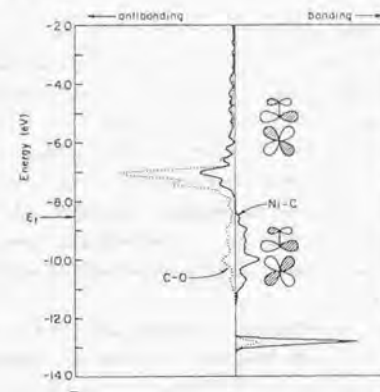


Figure 2.3: The crystal orbital overlap population curve for the CO/Ni(100) $c(2 \times 2)$ system with respect to the Ni-C (solid line) and C-O (dotted line) bonds. After Ref. [40].

Calculations by Hoffmann's group are, however, based on the extended Hückel method, which is a semi-empirical and very approximate way of calculating electronic structures and often yields even qualitatively incorrect results. One of the major deficiencies of the method is the lack of self-consistency. Self-consistency in the context of DFT-LDA calculations implies that the "input" effective-potential in the Kohn-Sham equation is identical to the "output" one that is obtained from the wavefunctions calculated for the Kohn-Sham equation with the "input" potential. A series of early self-consistent DFT-LDA calculations stressed that the self-consistency is of great importance for obtaining reliable results [41, 42, 43, 44, 45].

2.2.3 An analysis scheme applicable to wavefunctions expanded with a plane wave basis set

The disadvantage regarding computational costs involved in the use of a

plane wave basis set has been greatly mitigated with the progress of powerful computers and efficient computational schemes, as discussed in Subsec. 2.1.2. There is another disadvantage associated with a plane wave basis set, that is, one cannot easily get chemical and local views from calculations with it. Well-established chemical analysis schemes such as Mulliken's population analysis and Hoffmann's COOP curve mentioned above can be straightforwardly applied only to wavefunctions expressed in terms of LCAO-type basis functions. Now that calculations with plane wave basis sets have proven so powerful, a chemical analysis scheme that is applicable to such calculations is clearly needed.

We propose a simple scheme of population analysis that is basically similar to the Mulliken population analysis but is applicable to wavefunctions expanded with a plane wave basis set [8]. The scheme is illustrated in the following by taking as an example the CO/Pt(111) system, which will be the topic of the next chapter, but it should be noted that chemical bonds in other systems can also be dealt with in the same manner.

Suppose that one is interested in the bonding between CO molecule and Pt(111) surface. The atoms in the unit cell for CO/Pt(111) are divided into two subsets, with one (subset *a*) including only the C and O atoms composing the CO molecule and the other (subset *b*) consisting of the rest of the atoms (which are all Pt atoms in the present case). Two subsystems, *A* and *B*, are then invoked that are described by repeated unit cells in which the atoms in the subsets *a* and *b*, respectively, are located at exactly the same positions as in the total system, i.e., the CO/Pt(111) system. We express each of the one-electron wavefunctions for the total system, $\{\psi_\mu\}$, in terms of a basis set consisting of the wavefunctions for both subsystems, $\{\chi_i^A\}$ and $\{\chi_j^B\}$, as

$$\psi_\mu = \sum_{i=1}^{N_A} c_{\mu i}^A \chi_i^A + \sum_{j=1}^{N_B} c_{\mu j}^B \chi_j^B, \quad (2.20)$$

where only the lowest N_A and N_B eigenstates of the subsystems are included in the basis set. $\{\chi_i^A\}$ and $\{\chi_j^B\}$ are calculated using the same cutoff energy and the same unit cell size as for $\{\psi_\mu\}$ so that all these wavefunctions are

expanded with the same set of plane waves, saving us from numerical integrations in calculating the overlap integrals between them. $N_A(N_B)$ is taken to be the number of wavefunctions that would be obtained in an LCAO calculation with a minimal basis set, since the inclusion of eigenstates higher in energy, which might have large amplitude in the region around which none of the atoms are present, would obviously contradict the original spirit of Mulliken's population analysis. In the present case, N_A and N_B are 8 and 36, respectively, since each of the C and O atoms would have 4 basis functions (1 for 2s and 3 for 2p) and each of the Pt atoms in the unit cell would have 6 basis functions (5 for 5d and 1 for 6s) in a minimal basis set. Note that the 1s electrons of C and O as well as the core electrons up to the 5p electrons of Pt are replaced by pseudopotentials. $\{\chi_i^A\}$ then consists of the 3 σ , 4 σ , 1 π , 5 σ , 2 π and 6 σ molecular orbitals of CO.

From Eq. (2.20) we get

$$\langle \chi_i^A | \psi_\mu \rangle = c_{\mu i}^A + \sum_j c_{\mu j}^B \langle \chi_i^A | \chi_j^B \rangle, \quad (2.21)$$

and

$$\langle \chi_j^B | \psi_\mu \rangle = \sum_i c_{\mu i}^A \langle \chi_j^B | \chi_i^A \rangle + c_{\mu j}^B. \quad (2.22)$$

The coefficients, $c_{\mu i}^A$ and $c_{\mu j}^B$, are obtained by

$$\mathbf{c}_\mu = \mathbf{A}^{-1} \mathbf{b}_\mu, \quad (2.23)$$

where \mathbf{c}_μ and \mathbf{b}_μ are the $(N_A + N_B)$ -dimensional column vectors whose k -th components are given by

$$(\mathbf{c}_\mu)_k = \begin{cases} c_{\mu k}^A & \text{for } 1 \leq k \leq N_A \\ c_{\mu, k-N_A}^B & \text{for } N_A + 1 \leq k \leq N_A + N_B, \end{cases} \quad (2.24)$$

and

$$(\mathbf{b}_\mu)_k = \begin{cases} \langle \chi_k^A | \psi_\mu \rangle & \text{for } 1 \leq k \leq N_A \\ \langle \chi_{k-N_A}^B | \psi_\mu \rangle & \text{for } N_A + 1 \leq k \leq N_A + N_B. \end{cases} \quad (2.25)$$

\mathbf{A} is the $(N_A + N_B) \times (N_A + N_B)$ matrix which can be expressed as a block matrix:

$$\mathbf{A} = \begin{pmatrix} \mathbf{I}_{N_A} & \mathbf{S} \\ \mathbf{S}^\dagger & \mathbf{I}_{N_B} \end{pmatrix}, \quad (2.26)$$

where \mathbf{I}_{N_A} and \mathbf{I}_{N_B} are the unity matrices with a dimension of N_A and N_B , respectively. \mathbf{S} is the $N_A \times N_B$ matrix whose (i, j) -component, S_{ij} , is given by the overlap integral $\langle \chi_i^A | \chi_j^B \rangle$.

The expression given by Eq. (2.20) usually works quite well and the norm of the function that equals the difference between a true wavefunction for the total system and its counterpart expressed as in Eq. (2.20) has been found to be less than 0.002 for most of the one-electron states in the case of the calculations for CO/Pt(111) described in the next chapter.

Once one gets the expansion coefficients, one can calculate various kinds of populations following their definitions given in Subsec. 2.2.1. In the case of CO/Pt(111), the gross population of each molecular orbital of CO, q_i^μ , and the overlap population with respect to the bond between CO and the surface, p^μ , are given by

$$q_i^\mu = |c_{\mu i}|^2 + \frac{1}{2} \left\{ \sum_j (c_{\mu i}^A)^* c_{\mu j}^B S_{ij} + (\text{complex conjugate}) \right\}, \quad (2.27)$$

and

$$p^\mu = \sum_{i,j} (c_{\mu i}^A)^* c_{\mu j}^B S_{ij} + (\text{complex conjugate}), \quad (2.28)$$

respectively, for each orbital ψ_μ of the total system. The total gross and overlap populations, q_i and p , are then given by

$$q_i = \sum_\mu n_\mu q_i^\mu, \quad (2.29)$$

and

$$p = \sum_\mu n_\mu p^\mu, \quad (2.30)$$

where n_μ is the occupation number of ψ_μ .

Note that the only parameters involved in the present analysis scheme are the numbers of the basis states, N_A and N_B , used to (re-)expand the wavefunctions obtained by an electronic structure calculation (see Eq. (2.20)). However, the gross and overlap populations calculated with the present scheme are such quantities as neither become more accurate (i.e., more physically reasonable) nor converge with increasing N_A and N_B , as mentioned above. Though there are in principle as many eigenstates as the number of the plane wave basis states, N_{pw} , for each of the subsystems A and B , the basis set used to (re-)expand the wavefunctions as in Eq. (2.20) would be obviously overcomplete if N_A and/or N_B were as large as N_{pw} .

The present population analysis scheme has several advantages in addition to its applicability to calculations with plane wave basis sets, which are described in the following.

1. In LCAO-type calculations, it is often the case that large-sized basis sets including diffuse basis functions have to be used to improve the accuracies of calculations. However, a Mulliken analysis performed with such a large basis set is in most cases misleading [46, 47, 48], since diffuse functions centered on one atom might be able to represent electrons that physically belong to other atoms. In performing a Mulliken analysis, one has to severely reduce the size of the basis set used, which in turn degrades the accuracy of the electronic structure calculation. In the present scheme, on the other hand, it is the energy cutoff of the plane wave basis set that determines the accuracy of the electronic structure calculation, while a minimal basis set can be used for the population analysis such that physically unreasonable results can be avoided.
2. The present scheme ensures that the sum of the total gross populations over all the basis functions, $\{\chi_i^A\}$ and $\{\chi_j^B\}$, is equal to the total number of electrons in the total system, thus enabling the interpretation of each gross population as the number of electrons assigned to each basis function. This is in contrast to the orbital projection scheme [49], where

the population $p(\phi)$ of an orbital of interest ϕ is taken to be given by

$$p(\phi) = \sum_{\mu} n_{\mu} |\langle \phi | \psi_{\mu} \rangle|^2. \quad (2.31)$$

The scheme has been applied to various systems to discuss the charge states of atoms and molecules [49, 50, 51, 52]. Projected density of states (PDOS) $N_{\phi}(\epsilon)$, which is given by

$$N_{\phi}(\epsilon) = \sum_{\mu} |\langle \phi | \psi_{\mu} \rangle|^2 \delta(\epsilon - \epsilon_{\mu}), \quad (2.32)$$

and which is often exploited in the solid state physics trade [53, 54], is also based on the same spirit as this scheme, and the integration of such PDOS up to the Fermi level yields $p(\phi)$ given in Eq. (2.31). However, such a quantity as $p(\phi)$ cannot be actually regarded as a kind of population, as can be readily illustrated by the following example of the hydrogen molecule. Its bonding orbital ψ_b is expressed as a linear combination of the 1s atomic orbitals of the two hydrogen atoms, χ_1 and χ_2 , as

$$\psi_b = \frac{1}{\sqrt{2(1+S)}} (\chi_1 + \chi_2), \quad (2.33)$$

where S is the overlap integral between them. Then both $|\langle \chi_1 | \psi_b \rangle|^2$ and $|\langle \chi_2 | \psi_b \rangle|^2$ are $(1+S)/2$, though they should be $1/2$ for such a perfectly covalent bond. The sum of those quantities is $1+S$, which deviates by S from the ideal value of 1 and clearly shows that they cannot be interpreted as the populations of the respective 1s atomic orbitals.

3. The present scheme enables population analyses in terms of molecular orbitals in a straightforward fashion, which are important especially for discussing molecular-orbital-based pictures of chemical bonds such as the Blyholder model for the bonding of CO to metal surfaces, that will be the topic of the next chapter. Few such population analyses, however, have been performed even in the context of LCAO-type calculations, since the conventional Mulliken analysis scheme yields only the

populations of atomic orbitals. Calculations for the populations of the molecular orbitals of interest necessarily involve the (re-)expansions of wavefunctions in terms of those molecular orbitals, as in the present scheme, and the calculation of the inverse of an overlap matrix is required.

Chapter 3

Chemisorption of CO on Pt(111): Validity of the Blyholder Model

3.1 Introduction

Carbon monoxide (CO) is one of the most extensively studied adsorbates, since understandings of its adsorption on metal surfaces are important from both industrial and fundamental viewpoints. From an industrial point of view, CO plays a crucial role in various catalytic reactions such as the Fisher-Tropsch synthesis, where hydrocarbons, which are the main ingredients of petroleum, are efficiently synthesized from reactions of CO and H₂ with a catalyst consisting of iron and cobalt. Fundamentally, since adsorption of CO can take place on a variety of surfaces, its systematic study has a possibility of offering a comprehensive understanding of chemisorption in general. Although CO adsorbs dissociatively on some surfaces, we focus on molecular chemisorption in this chapter.

The electronic structure of the gaseous (i.e., free) CO molecule is illustrated in Fig. 3.1. The electronic configuration of the $^1\Sigma^+$ ground state of

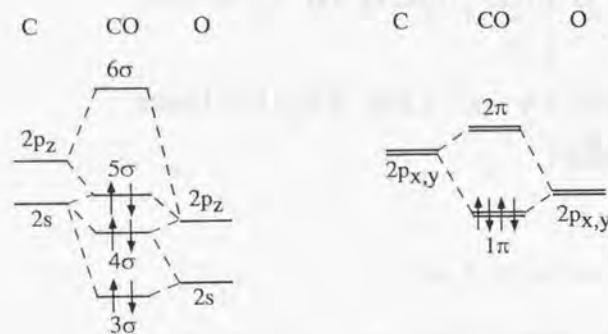


Figure 3.1: Schematic illustration of how the atomic orbitals of C and O combine to yield the molecular orbitals of CO with the σ (left) and π (right) symmetries. The z -axis is taken to be in the direction of the molecular bond.

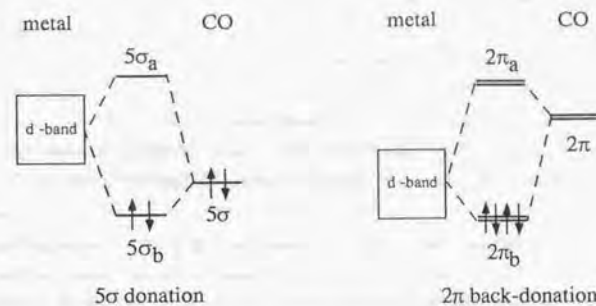


Figure 3.2: Schematic illustration of the Blyholder model, which describes the CO chemisorption via the 5σ donation (left) and the 2π back-donation (right).

CO is:

$$(1\sigma)^2(2\sigma)^2(3\sigma)^2(4\sigma)^2(1\pi)^4(5\sigma)^2.$$

The highest occupied molecular orbital (HOMO) and lowest unoccupied molecular orbital (LUMO) are 5σ and 2π , respectively.

The bonding of CO to transition metal surfaces has been understood in terms of the Blyholder model, which is based on the frontier orbital theory in that only the HOMO and LUMO of CO molecule play a role in the bonding. In this model, the bonding is considered to result from two contributions, namely the 5σ donation and the 2π backdonation. These are schematically illustrated in Fig. 3.2. The 5σ orbital splits into bonding ($5\sigma_b$) and antibonding ($5\sigma_a$) levels by the interaction with the metal bands. The $5\sigma_b$ level has mainly the molecular character, while the metal character is dominant for the $5\sigma_a$ level. Since $5\sigma_a$ is located above the Fermi level and thus unoccupied, the 5σ orbital, which is completely filled in the gas-phase, becomes partially empty. Since this implies that an electron is transferred (or donated) from the

5σ orbital to the metal, such an effect is called the 5σ donation. In a similar way, the 2π orbital interacts with the metal bands to split into bonding ($2\pi_b$) and anti-bonding ($2\pi_a$) levels. By populating electrons in the $2\pi_b$ level (with predominantly metallic character), partial occupation of the 2π orbital is attained, which is called the 2π backdonation. Because the Blyholder model presents a simple and clear view of the chemisorption bond, numerous experimental as well as theoretical data have been interpreted based on this model.

However, no clear evidence of the 5σ donation and 2π backdonation has been presented so far. There has been much effort to detect occupied 2π -derived states (corresponding to the $2\pi_b$ level in the simplified picture shown in Fig. 3.2), since the verification of their existence would imply the 2π backdonation and support the Blyholder model. Ultraviolet photoemission spectroscopy (UPS) studies exhibited weak features 0-2 eV below the Fermi level for Ni [55] and Cu [56] surfaces, which were considered to correspond to the $2\pi_b$ level. However, Miranda et al. showed for CO/Pd(110) that a feature just below the Fermi level observed in UPS does not stem from the 2π orbital of CO, but from a shifted Pd surface state [57]. Also, there have been attempts to find unoccupied 5σ -derived states (corresponding to the $5\sigma_a$) by means of inverse photoemission spectroscopy. Although Rangelov et al. ascribed a feature in their spectra for CO/Pt(110) to the $5\sigma_a$ contribution [58], no decisive evidence justifying such an assignment was given. Such difficulties involved in the detection of the $2\pi_b$ and $5\sigma_a$ levels are derived from their predominantly metallic character.

Several studies have cast doubts upon the adequacy of the Blyholder model. Wong et al. performed a semi-empirical extended Hückel calculation for CO/Pt(111), and showed that upon adsorption the 4σ orbital also becomes partially empty as well as the 5σ orbital [13]. The calculated electron occupation numbers of the 4σ , 5σ and 2π orbitals are 1.84, 1.54 and 0.38, respectively, for CO adsorbed at on-top sites of Pt(111). From these results, they argued that the 4σ orbital also plays a role in the formation of the chemisorption bond. Recently, X-ray emission spectroscopy (XES)

experiments by Nilsson et al. for CO/Ni(100) [11] (and also for N_2 /Ni(100) [11, 12], where the adsorption mechanism of N_2 is expected to be similar to that of the isoelectronic CO) showed the existence of occupied states with the π symmetry that are localized on one of the atoms in the molecule. Since the molecular orbitals of CO with the π symmetry, 1π and 2π , are extended over the molecule in the gas phase, they have claimed that it is inappropriate to describe the electronic structure of the adsorption system in terms of the molecular orbitals, as in the Blyholder model.

In this chapter, we reexamine the adequacy of the Blyholder model using the state-of-the-art first-principles calculations combined with the new population analysis scheme [8]. Most of the previous calculations addressing this problem are either calculations with clusters to model the adsorption systems or those with slabs but based upon semi-empirical methods such as the extended Hückel method. Recently, Hu et al. studied the electronic structure of CO/Pd(110) by means of a first-principles calculation with a slab model and a plane wave basis set, an approach similar to ours [14]. In order to discuss the Blyholder model, however, they examined the charge density distribution of *all* the calculated one-electron orbitals. The population analysis scheme adopted here saves such troublesome procedures and also allows more quantitative discussions. We study CO/Pt(111) in the present chapter because there has been a wealth of experimental as well as theoretical work on this system concerning not only static properties such as the adsorption geometry [59, 60, 61] and the electronic state [62, 63, 53, 54] in the ground state, but also dynamical properties which manifest themselves in, e.g., photo-induced desorption [64, 65, 66, 38, 39].

3.2 Electronic structure of gaseous CO

Before discussing the electronic structure of CO/Pt(111), we first examine that of the gaseous CO in this section. Such an isolated molecule can also be studied by means of a calculation with a plane wave basis set by introducing a supercell that is sufficiently large to make the (artificial) inter-

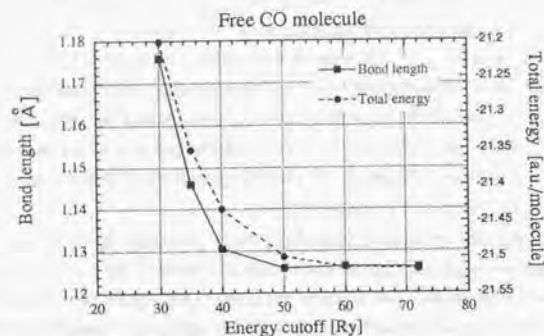


Figure 3.3: The dependence of the equilibrium C-O bond length (solid line) and total energy (dashed line) of the gaseous CO molecule upon the energy cutoff of the plane wave basis set.

actions between neighboring molecules negligible. Only the Γ point in the Brillouin zone is explicitly treated in the calculations. Figure 3.3 displays the dependence of the equilibrium C-O bond length and total energy upon the energy cutoff of the plane wave basis set. The equilibrium bond length converges faster than the total energy with respect to the energy cutoff, since the former is associated with the relative total energy as a function of the C-O distance. We usually need information only on the *relative* total energy such as the energy difference between two different atomic configurations rather than on the *absolute* total energy. For such information, an energy cutoff of 50 Ry, or even 40 Ry, suffices, as is apparent from Fig. 3.3. The results presented in this section have been obtained with an energy cutoff of 50 Ry. The equilibrium C-O bond length calculated with this energy cutoff, which is almost equal to the converged value, is 1.126 Å, in excellent agreement with the experimental value of 1.128 Å. However, the calculated orbital energies deviate significantly from the experimental values obtained with UPS mea-

molecular orbital	orbital energy [eV]	
	calc.	exp.
3σ	-28.8	—
4σ	-13.7	-19.7
1π	-11.6	-16.5
5σ	-8.7	-14.0
2π	-1.7	—

Table 3.1: The calculated orbital energies of the molecular orbitals of the gaseous CO. The corresponding experimental values obtained with ultraviolet photoemission spectroscopy (from Ref. [67]) are also presented. Note that the 1π and 2π are doubly degenerate.

surements [67], as shown in Table 3.1. This might be attributed to orbital relaxation effects involved in UPS processes, in which orbitals are affected by the removal of an electron. Such effects manifest themselves in the case of small molecules, but is expected to be insignificant for extended systems. The calculated relative energy positions of the 4σ , 1π and 5σ orbitals appear to be in rough accord with experiment.

A population analysis is performed by means of the scheme introduced in Subsec. 2.2.3. The CO molecule is divided into the C and O atoms, which correspond to the subsystems A and B following the notations used in Subsec. 2.2.3. Both N_A and N_B are taken to be 4 (1 for 2s and 3 for 2p). The results of the population analysis are summarized in Table 3.2. For simple homopolar molecules the 2s orbitals of the two atoms would interact with each other to form bonding 3σ and anti-bonding 4σ orbitals. This is not the case for CO. Both the 3σ and 4σ consist mainly of the contributions from the oxygen, while the 5σ is derived predominantly from the carbon. The overlap population of the 5σ orbital implies that the orbital has anti-bonding character, though it has been thought to have almost non-bonding character. (The CO^+ ion formed by the removal of a 5σ electron exhibits a C-O stretching frequency of 2200 cm^{-1} [67] and a bond length of 1.115 Å

molecular orbital	gross population		overlap population
	C	O	
3 σ	0.21	0.79	0.31
4 σ	0.11	0.89	-0.02
1 π	0.27	0.73	0.22
5 σ	0.93	0.07	-0.29
2 π	0.74	0.26	-0.52

Table 3.2: The gross populations of the C and O atoms as well as the C 2s, C 2p, O 2s and O 2p atomic orbitals and the overlap populations with respect to the C-O bond are presented for each molecular orbital of the gaseous CO.

[68], which are almost the same as the values of 2157 cm^{-1} and 1.128 Å for the neutral CO.) The discrepancy might also be attributed to orbital relaxation effects. As can be seen from Table 3.2, however, the 2 π orbitals are much more anti-bonding than the 5 σ orbital, and their population through the 2 π backdonation plays a crucial role in determining the C-O bond strength when CO adsorbs on a variety of surfaces.

Recently, X-ray emission spectroscopy has developed and become of great use for investigating the contributions from each atom composing a molecule to each molecular orbital. In the case of CO, one first creates a 1s core hole of the carbon, for instance. One then detects an X-ray emission due to the electronic transition from a valence molecular orbital of CO to the core hole. The transition matrix element is proportional to the overlap integral between the valence MO and the carbon 1s atomic orbital. Due to the selection rule, only the C 2p contribution to the MO is extracted. The same procedure goes for the oxygen. Figure 3.4 shows such spectra obtained for the gaseous CO by Skytt and co-workers [69]. The "non-resonant" spectra in Fig. 3.4 should be compared to the gross populations of the C 2p and O 2p atomic orbitals presented in Table 3.3. Since the atomic populations reproduce well the qualitative features of the experimental spectra, we can see that the population analysis goes well.

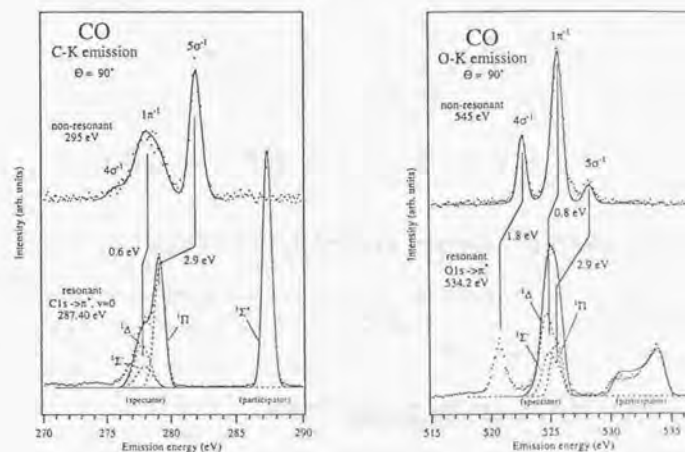


Figure 3.4: X-ray emission spectra observed for the gaseous CO by creating a C 1s (left) or O 1s (right) core hole. The curves designated as "non-resonant" and "resonant" are spectra observed by exciting a core electron to the unbound continuum and a bound unoccupied orbital, respectively. The "non-resonant" spectra should be compared to the results of the population analysis. The presence of an electron in an unoccupied orbital complicates the "resonant" spectra. After Ref. [69].

molecular orbital	gross population			
	C 2s	C 2p	O 2s	O 2p
3 σ	0.10	0.11	0.67	0.12
4 σ	0.12	-0.01	0.26	0.63
1 π	0.00	0.27	0.00	0.73
5 σ	0.62	0.31	0.00	0.07
2 π	0.00	0.74	0.00	0.26

Table 3.3: The gross populations of the C 2s, C 2p, O 2s and O 2p atomic orbitals for each molecular orbital of the gaseous CO.

3.3 Electronic structure of CO/Pt(111)

In this section, we investigate the electronic structure of CO/Pt(111) by the DFT-LDA electronic structure calculation and the population analysis scheme described in Subsec. 2.2.3.

3.3.1 Computational conditions

Total energy calculations were performed based on the density functional theory (DFT) with the local density approximation (LDA) for the exchange-correlation energy functional. Ab initio pseudopotentials in the separable form [30] which were generated with the Troullier-Martins procedure [31] were employed for all the atoms, namely, Pt, C and O. A plane wave basis set with an energy cutoff of 40 Ry was used. As can be seen from Fig. 3.3, the energy cutoff of 40 Ry suffices to produce reasonably reliable results for the gaseous CO. The equilibrium C-O bond length obtained with this energy cutoff is 1.131 Å, which is close to the converged value of 1.126 Å. As for Pt, we performed test calculations for bulk Pt, and found that this energy cutoff yields an optimized lattice constant of 4.00 Å, which is almost identical to the converged value of 4.01 Å. Thus calculations with the energy cutoff of 40 Ry are also expected to give reliable results for CO/Pt(111). Note that the experimental value for the lattice constant of bulk Pt is 3.92 Å. Thus our

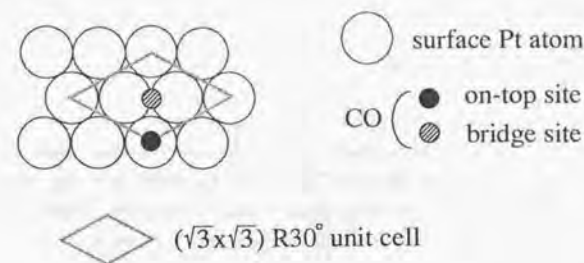


Figure 3.5: The $(\sqrt{3} \times \sqrt{3})R30^\circ$ unit cell used in the calculations. There is one CO molecule per unit cell, corresponding to a coverage of 1/3. The solid and hatched circles represent on-top and 2-fold bridge sites, respectively.

calculations overestimate it by about 2%.

16 uniform k-points were employed to sample the surface Brillouin zone. Since LEED studies showed the $(\sqrt{3} \times \sqrt{3})R30^\circ$ pattern up to a coverage of one third [59, 61], we adopted the $(\sqrt{3} \times \sqrt{3})R30^\circ$ unit cell with one CO molecule in it, which corresponds to a coverage of one third. The unit cell used is displayed in Fig. 3.5. The lattice constant used to construct the unit cell is taken to be the calculated value of 4.00 Å rather than the experimental value. The surface is approximated by a slab composed of 2 layers of Pt to save the computational costs. A study on the dependence of the adsorption energy for CO/Cu(100) upon the number of surface layers [36] suggested that even 2 layers suffice to give reasonably accurate results, as has been shown in Table 2.1. We investigated CO adsorbed at on-top sites since EELS [60] and IRAS [61] measurements have indicated the presence of only the on-top species at low coverages. Note that it has been shown that the 2-fold bridge species begin to appear as the coverage increases. It has been known that CO adsorbs with the C-end down. Thus geometrical optimization procedures started from such an atomic configuration. As a result of the structural

optimization, we found that the optimal C-O and Pt-C distances are 1.143 and 1.859 Å, respectively. As noted above, the calculated equilibrium C-O bond length for the gas-phase CO is 1.131 Å, and it can be seen that the C-O bond length is elongated slightly upon adsorption. A population analysis was performed following the procedures described in Subsec. 2.2.3. The CO/Pt(111) system was divided into the CO molecule (the subsystem A) and the Pt surface (the subsystem B). N_A and N_B in Eq. 2.20 were taken to be 8 and 36. The former corresponds to a minimal basis set consisting of C 2s, C2p, O 2s and O 2p, and the latter to that of Pt 5d and Pt 6s.

3.3.2 Results and Discussions

Figure 3.6 shows the total density of states (DOS) for CO adsorbed at on-top sites of Pt(111), where one can see three prominent CO-derived peaks below the Pt d bands, which are located -10.1, -7.8 and -7.0 eV relative to the Fermi level. Note that values of energies indicated in this subsection are all relative to the Fermi level. In UPS measurements such three peaks are actually observed for CO adsorbed on a variety of transition metal surfaces [10, 57, 62]. They are usually identified as derived from the 4σ , 5σ and 1π molecular orbitals in the order of increasing energy. The locations of such three peaks observed in a UPS study for CO/Pt(111) [62] are -11.9, -9.2 and -8.4 eV, which are in rough accord with the above calculated values.

Figure 3.7 shows the curves representing the DOS weighted by the gross populations of the CO 4σ and 5σ orbitals. One can clearly see from Fig. 3.7 that the lower two of the three peaks seen in the total DOS are derived from the 4σ and 5σ orbitals. However, our results show that they are neither purely 4σ - nor 5σ - derived states, but have contributions from both molecular orbitals, implying that these orbitals rehybridize with each other upon adsorption. Similar results were obtained by Hammer et al., who calculated the 5σ -projected DOS for CO/Pt(111) [53]. Note that two peaks seen in this DOS, which were calculated with a slab composed of 6 surface layers, are located at almost the same energies as in the present calculation, suggesting that the slab of 2 surface layers we used is sufficient to yield reliable results.

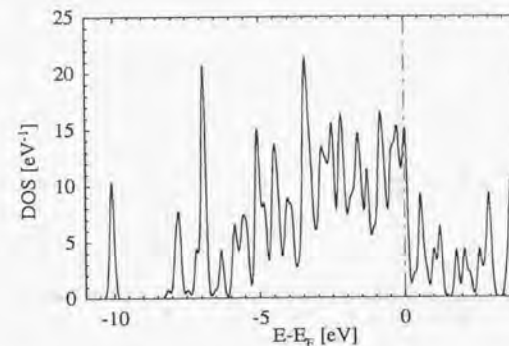


Figure 3.6: The total density of states calculated for CO adsorbed at on-top sites of Pt(111).

As will be shown below, the peak at -7.0 eV in the total DOS consists mainly of a contribution from the 1π orbital. While the 5σ orbital is higher in energy than the 1π in the gas phase, UPS studies have shown that the peak which has been thought to be derived from the 5σ (denoted by $5\bar{\sigma}$ hereafter) becomes energetically lower than the 1π -derived peak in the adsorbed state. The lowering of the $5\bar{\sigma}$ peak has been regarded as an indication that the $5\bar{\sigma}$ orbital is involved in the formation of the chemisorption bond. Ishi et al. claimed that the lowering of the $5\bar{\sigma}$ peak is due to a lengthening of the C-O bond upon adsorption rather than the bonding interaction of the $5\bar{\sigma}$ with the metal bands [10]. However, this is not the case at least for CO/Pt(111), since calculations we performed for the isolated CO molecule have shown that the elongation of the bond length from 1.131 Å to 1.143 Å upon adsorption leads to a lowering of the $5\bar{\sigma}$ level only by 0.03 eV. From Fig. 3.7 one can see that the $5\bar{\sigma}$ peak is actually derived from a mixture of the 4σ and 5σ orbitals, and the fact that this peak gets lower than the 1π -derived one is partly attributed

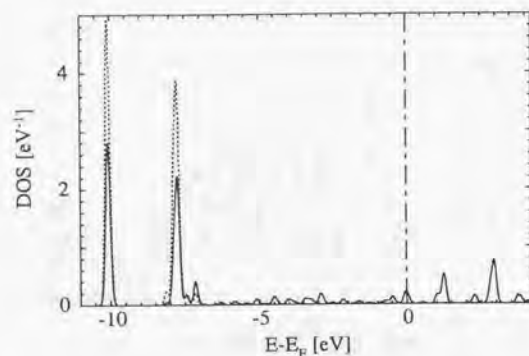


Figure 3.7: The density of states weighted by the gross populations of the CO 4σ (dashed line) and 5σ (solid line) orbitals.

to the mixing of the 5σ with the lower-lying 4σ . Of course, this does not necessarily deny the involvement of the 5σ orbital in the bonding.

It is apparent from Fig. 3.7 that above the Fermi level there are almost no 4σ contributions, while significant 5σ contributions can be seen. The integrations of the DOS curves shown in Fig. 3.7 up to the Fermi level give the total gross populations of the 4σ and 5σ orbitals in the ground state, which are calculated to be 2.00 and 1.47, respectively. They are listed in Table 3.4 together with the total gross populations of the other molecular orbitals of CO. Since the 4σ orbital is completely filled, it does not play a role in the bonding of CO to the surface. This is in contrast to the result of the extended Hückel calculation [13], which is considered to be less reliable due to its semi-empirical nature than the present *ab initio* result. On the other hand, the 5σ contributes much to the bonding through the donation of 0.53 electrons.

The DOS curves weighted by the gross populations of the CO 1π and 2π

molecular orbital	gross population	overlap population
3σ	2.00	-0.01
4σ	2.00	-0.01
1π	4.00	-0.08
5σ	1.47	0.39
2π	0.52	0.51
6σ	0.02	0.01
total	10.01	0.81

Table 3.4: The gross and overlap populations associated with each molecular orbital of CO are shown together with the corresponding total populations. The overlap populations are calculated for the Pt-CO bond. The total gross population indicates that CO is almost neutral (-0.01 e negatively charged) on Pt(111).

orbitals are presented in Fig. 3.8. The total gross populations are 4.00 and 0.52 for the 1π and 2π orbitals, respectively, as shown in Table 3.4. The 1π orbitals are completely filled and do not contribute to the bonding of CO to the surface. In contrast to the 4σ orbital, which is also completely filled, the 1π orbitals interact with the metal bands and states with some 1π contributions, which range from -6 to -1 eV, can be seen within the metal bands besides the strong 1π -derived peak at -7 eV. The backdonation of 0.52 electrons to the 2π orbitals is attributed to the occupied states with the 2π contributions that can be seen in Fig. 3.8. They are distributed in a wide energy range, suggesting the strong interaction of the 2π orbitals with the metal bands. Since the 2π -derived states are spread in energy, the intensity of these energy levels in, e.g., UPS, should be weak. Thus the peaks of the occupied 2π states are buried in strong features from the metal bands and are hardly observed in UPS measurements [10, 57].

Figure 3.9 shows the calculated COOP curve with respect to the bond between the CO and the surface. A positive (negative) value of the curve

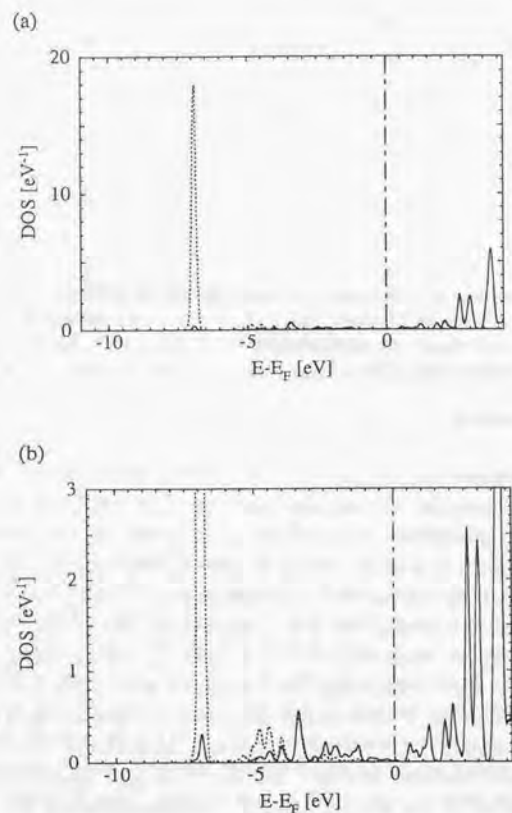


Figure 3.8: The density of states weighted by the gross populations of the CO 1π (dashed line) and 2π (solid line) orbitals. (a) and (b) are different in the range of the ordinate.

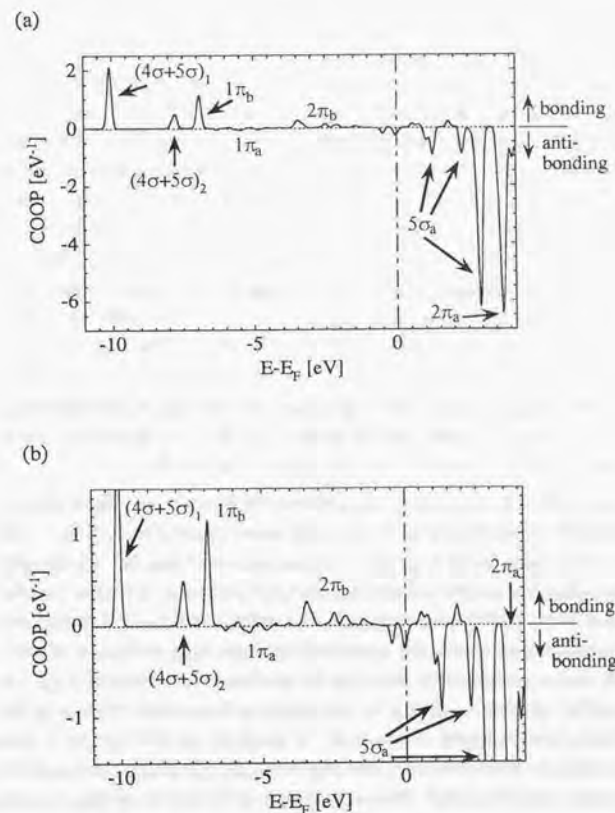


Figure 3.9: The crystal orbital overlap population (COOP) curve with respect to the bond between the CO and the Pt(111) surface. Positive and negative values indicate bonding and antibonding contributions to the bond, respectively. (a) and (b) are different in the range of the ordinate.

at an energy indicate that the one-electron states with that energy give a bonding (antibonding) contribution to the chemisorption bond. The integration of the COOP curve up to the Fermi level yields the total overlap population, which can serve as a measure of the strength of the chemisorption bond. The calculated total overlap population is 0.81. By comparison with the gross population weighted DOS shown in Figures 3.7 and 3.8, we can readily identify the character of each peak in the COOP curve, which is also indicated in Fig. 3.9. One can see the prominent bonding contributions from the three peaks located at -10.1, -7.8 and -7.0 eV, which we designate as $(4\sigma + 5\sigma)_1$, $(4\sigma + 5\sigma)_2$ and $1\pi_b$ in Fig. 3.9, respectively, where the subscript b implies a bonding orbital. However, one cannot conclude from this that all the 4σ , 5σ and 1π orbitals contribute to the chemisorption bond, since if both the bonding and anti-bonding levels derived from an orbital are occupied, then the net contribution from the orbital is non-bonding or even repulsive. As discussed above based upon the calculated gross population of each orbital, that is the case for the 4σ and 1π . In contrast, the partially filled 5σ and 2π are considered to be involved in the bonding.

The same conclusion as mentioned above can be more clearly drawn by investigating the contributions from each molecular orbital of CO to the COOP curve displayed in Fig. 3.9. As can be seen from Eq. (2.28), the overlap populations used to calculate the COOP curve are sums over all the molecular orbitals of CO (represented by the index j in Eq. (2.28)), and can be readily decomposed into the contributions from each molecular orbital. The DOS curves weighted by the overlap populations associated with the CO 4σ and 5σ orbitals, namely, the contributions from these orbitals to the COOP curve, are presented in Fig. 3.10. It is apparent that the $(4\sigma + 5\sigma)_1$ peak has a mixed character of $4\sigma_b$ and $5\sigma_b$, while the $(4\sigma + 5\sigma)_2$ peak consists of $4\sigma_a$ and $5\sigma_b$ contributions. The integrations of the curves in Fig. 3.11 up to the Fermi level yield -0.01 and 0.39 for 4σ and 5σ , respectively, which are listed in Table 3.4. These indicate again that the 4σ is irrelevant to the chemisorption bond, while the 5σ contributes much to the bond.

Figure 3.11 displays the DOS curves weighted by the overlap populations

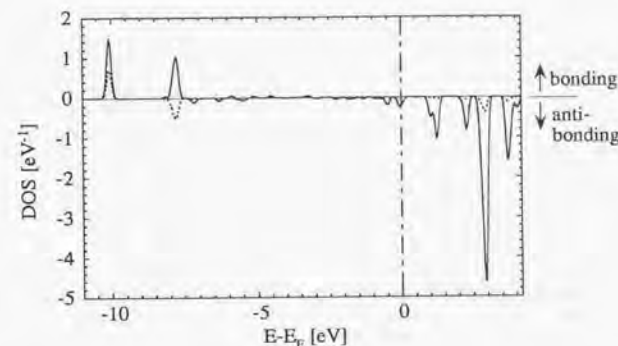


Figure 3.10: The density of states weighted by the overlap populations associated with the CO 4σ (dashed line) and 5σ (solid line) orbitals.

associated with the CO 1π and 2π orbitals. As is apparent from Fig. 3.8, states located in the energy range from about -6 to -1 eV have contributions from both the 1π and 2π orbitals with the ratio of the former to the latter decreasing with increasing energy. Figure 3.11 clearly indicates that the 1π and 2π orbitals give antibonding and bonding contributions (with regard to the Pt-CO bond), respectively, to the states in this energy range, resulting in net antibonding character (denoted by $1\pi_a$) between -6 and -4 eV and net bonding character (denoted by $2\pi_b$) between -4 and -1 eV in the COOP curve displayed in Fig. 3.9. By integrating the curves in Fig. 3.11 up to the Fermi level, we obtain the contributions from the 1π and 2π orbitals to the total overlap population, which are calculated to be -0.08 and 0.51, respectively. It can be seen once again from these values that the completely filled 1π orbital is not involved in the bonding, while the 2π plays a crucial role.

As a result of the mixing of the 1π and 2π orbitals in the energy range from -6 to -1 eV as discussed above, it is possible that states localized on

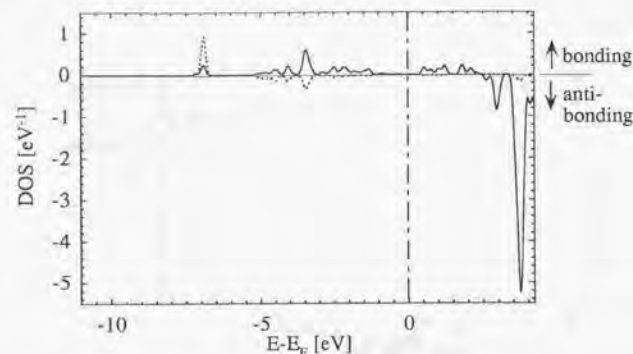


Figure 3.11: The density of states weighted by the overlap populations associated with the CO 1π (dashed line) and 2π (solid line) orbitals.

either of the C and O atoms of the CO molecule are formed, as observed in an XES experiment [11]. Figure 3.12 shows the DOS curves weighted by the gross populations of the C and O $2p$ atomic orbitals. They can be considered to correspond to the XES data in Ref. [11], which are shown in Fig. 3.13 for comparison. Note that the XES measurement was performed for CO/Ni(100) and that the data were separated into the contributions from the states with the σ and π symmetries. In calculating the gross populations of these atomic orbitals, the population analysis scheme described in Subsec. 2.2.3 was employed with the system divided into three parts, that is, the C atom, the O atom and the rest of the system. As expected, in the energy range between -6 and -3 eV, states with much larger amplitudes of the O $2p$ orbitals than those of the C $2p$ orbitals can be seen. The contribution of the C $2p$ orbitals increases as the energy level increases and becomes comparable to the O $2p$ contribution just below the Fermi level. Therefore we agree with Nilsson et al. in that the new model they came up with [11, 12], which

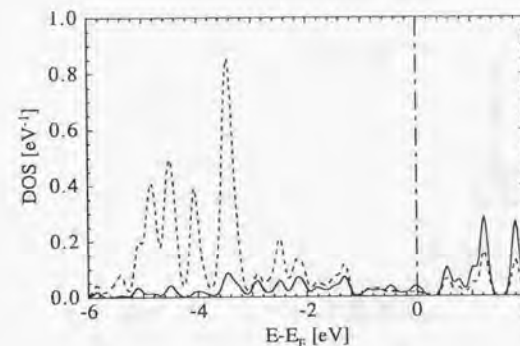


Figure 3.12: The density of states weighted by the gross populations of the C $2p$ (solid line) and O $2p$ (dashed line) orbitals.

is an atomic-orbital-based picture, is appropriate for describing some of the one-electron states of the adsorbed system. We would like to claim, however, that the molecular orbitals of CO can be the most appropriate basis orbitals for a simple understanding of the mechanism of CO chemisorption, since, as discussed above, only two of the molecular orbitals, namely 5σ and 2π , contribute to the bonding from the viewpoint of the molecular-orbital-based picture, i.e., the Blyholder model.

Information on unoccupied states obtained from Fig. 3.9 can be of great use in gaining insight into several experiments. Rangelov et al. observed inverse photoemission spectra for CO/Ni(110), CO/Pd(110) and CO/Pt(110) [58]. One of the unoccupied bands observed for CO/Pt(110), which is located below some 2π -derived bands, exhibits a band dispersion quite different from that expected for 2π -derived bands and they inferred that this band has the $5\sigma_a$ character. Confirmation of the existence of unoccupied states with the $5\sigma_a$ character is important as it is indicative of the 5σ donation. Figure 3.9

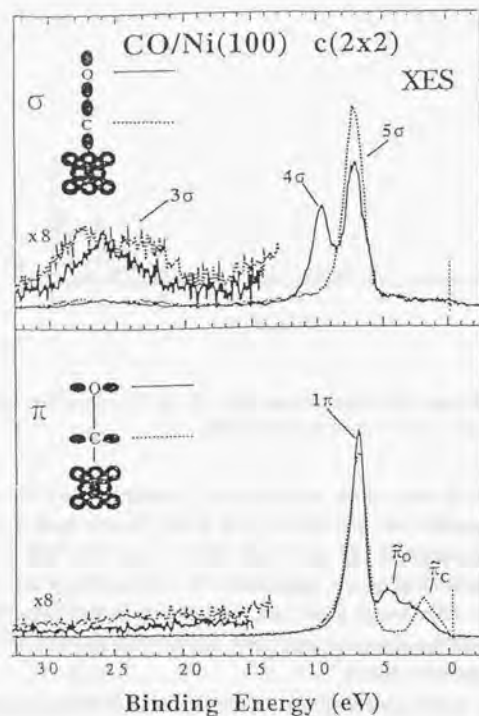


Figure 3.13: X-ray emission spectra observed for CO/Ni(100). The data for the states with the σ (upper panel) and π (lower panel) symmetries are separately shown. After Ref. [11].

clearly indicates the presence of unoccupied states with the $5\sigma_a$ character below states with the $2\pi_a$ character, supporting the above conjecture made by Rangelov et al., though our calculations have been performed for the (111) surface. Fukutani et al. investigated CO on a Pt(111)-Ge alloy and showed that the desorption energy of CO is greatly reduced compared to that for the clean Pt(111) surface, while the C-O stretching frequency remains almost constant [65]. They considered that alloying of Pt with Ge leads to an additional filling of the Pt d band. As is apparent from Fig. 3.9, additional electrons provided by Ge populate the states with the $5\sigma_a$ character prior to those with the $2\pi_a$ character. It is then expected that the chemisorption bond is weakened via the reduced 5σ donation, while the strength of the C-O bond remains almost constant, not only because the unoccupied states with the $5\sigma_a$ character are derived mainly from the metal states, but also because the population of the 5σ orbital in the gas-phase CO affects the bond strength much less than that of the 2π orbitals.

3.4 Summary

In this chapter, we have addressed the question as to whether the Blyholder model for the chemisorption of CO on transition metal surfaces, upon which several recent studies have cast doubts, is valid or not. For that purpose, we have performed DFT-LDA electronic structure calculations for CO/Pt(111) and analyzed the obtained data by means of the newly-developed population analysis scheme.

Prior to discussing the results for CO/Pt(111), we have applied the scheme to the gaseous CO and found that the calculated gross populations of C and O 2p atomic orbitals reproduce well observed X-ray emission spectra for the gaseous CO, which ensures that the scheme works quite well.

We have then applied the scheme to CO/Pt(111). The calculated gross populations of the molecular orbitals of CO have indicated that the 4σ and 1π are completely filled, while the 5σ and 2π are partially filled, suggesting that only the latter two orbitals contribute to the bonding of CO to

the surface. This has been more convincingly shown by examining the overlap populations associated with each molecular orbital. The π -symmetry states localized on either of the C and O atoms that were observed by an X-ray emission spectroscopy study have been reproduced by our calculations. Though this implies the need for an atomic-orbital-based picture to describe some individual one-electron states, the results of our population analysis mentioned above have definitely shown that the Blyholder model, which is a molecular-orbital-based picture, provides a lucid and essential way of describing the chemisorption bond, since one can discuss the bonding in terms of only two molecular orbitals.

Chapter 4

Etching processes of Si(100) with adsorbed halogens and hydrogens

4.1 Introduction

Halogen-adsorbed Si surfaces have been extensively studied, not only because of their fundamental interest as simple chemisorption systems involving semiconductor surfaces, but also because of their great technological significance. Halogen-containing plasmas are frequently used in etching of semiconductor surfaces [70, 71], which plays a crucial role in manufacturing semiconductor devices. Also, chlorine-adsorbed Si surfaces have been known to be susceptible to etching under laser irradiation [72, 73, 74, 75], and a full understanding of such laser-induced etching is expected to allow controlled local modifications of semiconductor surfaces. Thus one of the major goals of studies on halogen-adsorbed Si surfaces is to gain those insights into etching processes that could be helpful in improving the device processing technology.

Since halogens are chemically similar to hydrogen in that they are both monovalent elements, it is reasonable to expect that the adsorption of halogens is similar to that of hydrogen. The surface structure of H/Si(100) has

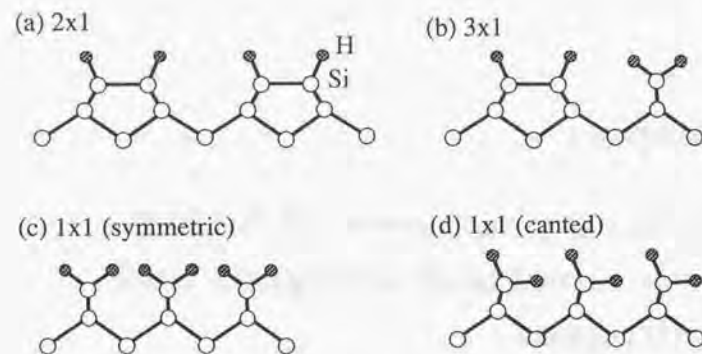


Figure 4.1: Schematic illustration of the (a) 2×1 , (b) 3×1 , (c) symmetric 1×1 and (d) canted 1×1 structures of H/Si(100).

been extensively studied, and three phases with 2×1 , 3×1 and 1×1 structures have been known to exist, whose hydrogen coverages are 1, $4/3$ and 2, respectively [76, 77]. They are schematically illustrated in Fig. 4.1. The 2×1 structure, which results from a moderate exposure of the clean Si(100) surface to the (atomic) hydrogen atmosphere, retains the 2×1 periodicity seen for the clean surface, with hydrogens saturating Si dangling bonds and forming monohydride dimers. The saturation H exposure at 380 K results in the 3×1 structure, which consists of alternating rows of monohydride dimer units and dihydride units [78]. With a further exposure at room temperature, the 1×1 phase, which is composed only of dihydride species, begins to be observed [79]. An *ab initio* calculation [80] showed that for the 1×1 phase the structure with canted dihydrides shown in Fig. 4.1(d) is energetically more favorable than the symmetric structure shown in Fig. 4.1(c), though the question as to which structure is realized remains unanswered experimentally.

In analogy to H/Si(100), halogen atoms are expected to saturate dangling

bonds of the clean Si(100) without disruption of the dimers for a moderate exposure to halogen gas. In fact, experimental [81, 82, 83, 16, 84] as well as theoretical [85, 86, 87] studies have been performed intensively to determine the adsorption sites of Cl atoms for Cl/Si(100), and all these studies agreed that the dangling bond site is the most favorable site, though some of them suggested the presence of another species which resides in between the two Si atoms of a dimer as a metastable state [83, 16, 84, 86]. Several experiments have also been performed for Br/Si(100) [88, 89, 90] and I/Si(100) [91], which have given similar results to those for Cl/Si(100), though there is few theoretical work concerning these systems except for a semi-empirical cluster calculation for Br/Si(100) [92]. Thus the Cl/Si(100), Br/Si(100) and I/Si(100) surfaces with a coverage of 1 ML are considered to assume a structure similar to that for H/Si(100) shown in Fig. 4.1(a).

As mentioned above, one of the main goals of investigations on halogen-adsorbed Si surfaces is to develop a microscopic understanding of etching processes so that better control of these processes could be accomplished. Etching generally consists of the following three steps: (1) Molecules in the gas phase are incident upon the surface. (2) The incident molecules react with substrate atoms to form volatile compounds. (3) The compounds are desorbed spontaneously or thermally. Thus experiments on etching usually monitor etching products (i.e., desorbed species) under continuous exposure of the surface to halogen gas [93, 94]. Such experiments involve all the three steps mentioned above and thus realistically simulate etching processes that are of technological relevance. However, results of such experiments are hard to interpret and do not provide a microscopic view of what is going on, as they are complicated by each of the three processes.

Several experiments have focused only on the step (3) above, i.e., the thermal desorption of silicon halides from halogen-adsorbed silicon surfaces. Although the surface structure is basically similar for the adsorption of the halogens and hydrogen as described above, completely different behaviors have been observed as regards etching. Thermal desorption studies for Cl/Si(100) [15, 16, 17] and Br/Si(100) [18, 19] have shown that the SiCl_2 and SiBr_2

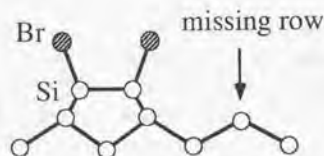


Figure 4.2: The atomic structure of the surface with 3×1 ordered missing rows.

species are among the dominant products, respectively. On the other hand, thermal desorption from H/Si(100) [20, 21] and I/Si(100) [18] yields mainly H_2 molecules and I atoms, respectively, with only a small fraction of silicon hydrides or iodides. This clearly shows that etching proceeds much more efficiently with the adsorption of Cl and Br than with that of H and I, though a microscopic mechanism of the etching (i.e., the desorption of the dihalides) has not been understood yet. Note that Jackman et al. found two peaks, called α and β , in thermal desorption spectra from Cl/Si(100), Br/Si(100) and I/Si(100) [15, 18]. As the exposure to halogen gas is increased, the β peak saturates in magnitude, while the α peak seems to continue developing without an apparent limit. Therefore they considered that the β peak represents chemisorbed species, while the α peak is indicative of the formation of a silicon halide corrosion phase. We discuss here only the desorption products corresponding to the well-defined β peak.

A candidate for an intermediate state of the etching process can be envisaged based on the results of an STM study by Chander et al. for Br/Si(100) [95]. They revealed that while exposure of the surface to Br_2 gas first produces a 2×1 monobromide structure, further exposure results in the appearance of 3×1 ordered missing rows. The 3×1 unit cell for this structure is composed of a monobromide dimer and a missing Si atom site, as shown in Fig. 4.2. Chander et al. proposed that this structure results from the desorption of the $SiBr_2$ species from the 3×1 surface as shown in Fig. 4.1(b), since the

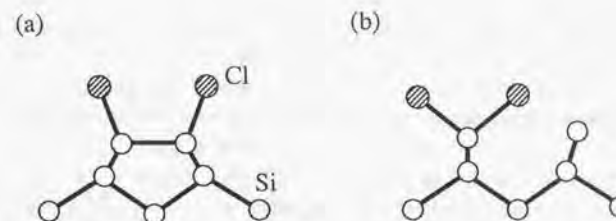


Figure 4.3: The atomic structures of the (a) initial and (b) final states of the isomerization reaction described in the text.

H/Si(100) surface, which should be chemically analogous to the Br/Si(100) surface, exhibits this structure under given conditions. Then, however, a remarkable difference with regard to etching manifests itself again between H and Br. For H the 3×1 surface is quite stable against etching, while for Br the $SiBr_2$ species are volatile and easily desorbed.

While the 3×1 surface is a possible candidate for an intermediate state of the thermal desorption of the dihalide species from high-coverage surfaces, de Wijs et al. proposed another mechanism for the desorption of $SiCl_2$, which can be operative even at low-coverage surfaces [96]. The mechanism involves a monochloride-dichloride isomerization reaction:



where the Cl atom attached to one Si atom of a dimer hops onto the other Si atom of the dimer. The initial and final states of the reaction are depicted in Fig. 4.3.

In this chapter, we investigate X/Si(100) ($X=H, Cl, Br$ or I) surfaces with first-principles electronic structure calculations and the population analysis scheme described in Subsec. 2.2.3. In Sec. 4.2, the calculational conditions adopted in the present chapter are described along with the test calculations we performed for checking the convergence of calculated quantities with re-

spect to a number of parameters. In Sec. 4.3, the monohalide (or monohydride) 2×1 surfaces as shown in Fig. 4.1(a), which are ubiquitously observed in experiments, are studied in order to gain insights into trends of the Si-X interactions. From Sec. 4.4 to Sec. 4.7, we discuss etching processes in which the SiX_2 species are (thermally) desorbed from the surface. We consider two kinds of the surfaces involving the SiX_2 species. One is the 3×1 surface as shown in Fig. 4.1(b) with a coverage of $4/3$ ML (Sec. 4.4) while the other is a 2×1 surface with a coverage of 1 ML which is similar to the surface shown in Fig. 4.3(b) (Sec. 4.5). By means of calculations of the desorption energies of the SiX_2 units from these surfaces as well as population analyses performed in the way described in Subsec. 2.2.3, we address the question as to why etching proceeds more efficiently with the adsorption of Cl and Br than with that of H and I. In Sec. 4.8, the H/Si(100) 1×1 surface, which is susceptible to etching in the presence of atomic hydrogen gas [76, 77], is briefly discussed.

4.2 Computational conditions

Total energy calculations were based upon the local density functional formalism. Ab initio pseudopotentials in the separable form [30] were employed. The pseudopotentials for Si and Cl are of the BHS type [33], while those for H, Br and I are of the TM type [31].

Wavefunctions were expanded in terms of a plane wave basis set with an energy cutoff of 18 Ry. In order to check the cutoff-dependence of calculated quantities, test calculations were performed for the SiX_4 molecules (X=H, Cl, Br and I). The equilibrium Si-X bond lengths for X=Cl, Br and I calculated with a cutoff of 18 Ry are 2.03, 2.21 and 2.45 Å, respectively, which do not vary appreciably as the cutoff is increased. Note that the corresponding experimental values are 2.01 ± 0.02 , 2.16 ± 0.03 and 2.43 ± 0.02 Å. On the other hand, the equilibrium Si-H bond length is calculated with a cutoff of 18 Ry to be 1.52 Å, which is slightly different from the converged value of 1.50 Å. (The experimental value is 1.48 Å.) However, we confirmed for H/Si(100) surfaces

that the calculated quantities of interest such as the desorption energies of SiH_2 and the overlap populations change little as the energy cutoff is raised from 18 Ry to 30 Ry. Note that an energy cutoff of at least 50 Ry was found to be required to perform calculations for F/Si(100) even with a TM soft pseudopotential for F, indicating that the use of an ultrasoft pseudopotential is necessitated for making them feasible.

We first performed geometrical optimizations without any symmetry constraints using sets of 12 and 8 k points for calculations with the 2×1 and 3×1 unit cells, respectively, and identified the symmetries that the optimized atomic configurations have. We then employed k point sets consisting of effective 48 and 32 k points for calculations with the 2×1 and 3×1 unit cells, respectively. By taking account of the symmetries found with the above geometrical optimizations, only 20 (15) k points among 48 (32) points should be explicitly treated for the 2×1 (3×1) unit cell. Since the calculated overlap populations were found to depend critically upon k , it first seemed that a large number of k points are required to obtain the converged values for the total overlap populations, the calculations of which involve sampling over k points. However, the quantities of interest (including the overlap populations) calculated with the 2×1 (3×1) unit cell did not vary significantly, as the number of k points was increased from 12 (8) to 48 (32), indicating that they are well converged as regards the k point sampling. All the quantities presented hereafter were those calculated with the sets of 48 and 32 k points for the 2×1 and 3×1 unit cells, respectively, unless otherwise stated. Note that these sets were taken to be equivalent to each other so that total energies calculated with the 2×1 and 3×1 unit cells can be compared directly.

We used supercells composed of a slab representing the surface and a vacuum region for separating slabs located repeatedly in the direction perpendicular to the surface. A vacuum region of about 7 Å was adopted, which was found to be thick enough by comparison with calculations with a vacuum region of more than 15 Å. The slab consists of 6 layers of Si, a layer of adsorbates on the upper surface and a layer of hydrogens that terminate dangling bonds of Si on the lower surface. Calculations with a slab including

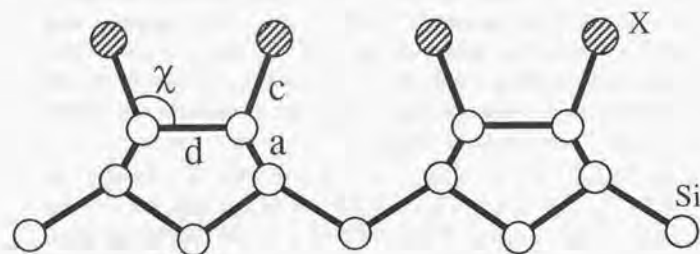


Figure 4.4: The definitions of some structural parameters characterizing the X/Si(100) 2×1 monohalide (or monohydride) surface.

10 layers of Si were also performed for some surfaces, the optimized surface structure being almost identical to that for the 6-layer slab.

4.3 2×1 monohalide/monohydride surfaces

Before discussing surfaces involving the SiX_2 species that might be directly related to etching processes, we first discuss the 2×1 monohalide (or monohydride) surfaces with a coverage of 1 ML (Fig. 4.1(a)), which are most frequently observed in experiments.

4.3.1 Surface structure

Several structural parameters for the optimized surfaces, whose definitions are illustrated in Fig. 4.4, are summarized in Table 4.1. Geometrical optimization procedures yielded surface structures consisting of *symmetrical* monohalide (or monohydride) dimers for all the adsorbates, in accord with experiments for the H/Si(100) [97], Cl/Si(100) [16] and Br/Si(100) [88] surfaces. Thus the adsorption of the halogens and hydrogen removes the tilt

X	c [Å]	χ [deg.]	d [Å]	a [Å]
H	1.54	110.5	2.41	2.35
Cl	2.07	109.2	2.42	2.35
Br	2.24	109.0	2.42	2.35
I	2.46	107.2	2.42	2.35

Table 4.1: The values of some structural parameters characterizing the optimized structure of the X/Si(100) 2×1 monohalide (or monohydride) surface with a coverage of 1 ML. For the definitions of the parameters, see Fig. 4.4.

of the Si dimers which is seen for the clean Si(100) surface. The lengths of the Si-Si backbonds, a , are almost constant for all the kinds of the adsorbates, while those of the Si-Si dimer bonds, d , are slightly longer for the three halogens than for hydrogen. This effect might be related to the large electronegativities of the halogens as compared to that of hydrogen. Note that the dimer bond length in the buckled dimer of the clean Si(100) surface is calculated to be 2.30 Å, which is considerably shorter reflecting the fact that the dimer bond has double-bond-like character. The lengths of the Si-X bonds, c , should be compared to those for the free SiX_4 molecules, which were calculated to be 1.52, 2.03, 2.21 and 2.45 Å for X=H, Cl, Br and I, respectively. As is apparent from Table 4.1, the bonds are slightly longer at the surfaces.

Slight variations can be seen for the angles between the Si-X bond and the Si-Si dimer bond, χ , among the different adsorbates. Since all the kinds of the adsorbates studied here (including hydrogen) have larger electronegativities than Si, they are considered to be negatively charged at the surface, resulting in the Coulomb repulsion between neighboring adsorbates. Thus the adsorbate atoms in a line perpendicular to the dimer row would arrange themselves so that the distances between the nearest-neighbor atoms are all equal (i.e. 3.84 Å), if it were not for the energy loss due to the strain of the Si-X bonds [88]. With the lengths of the Si-Si dimer bonds and the Si-X bonds presented in Table 4.1, the angles χ would be 117.8°, 110.1°, 108.5°

X	E_{mol} [eV]	E_{atom} [eV]
H	2.19	3.5
Cl	5.35	3.9
Br	4.58	3.3
I	3.62	2.6

Table 4.2: The desorption energies of X_2 molecules, E_{mol} , and X atoms, E_{atom} .

and 106.8° for X=H, Cl, Br and I, respectively. Actually, there is a tendency to avoid the bond-strain, keeping χ close to the optimal angle, which is the tetrahedral angle of 109.5° . This effect reduces χ for X=H from 118° to 111° . In the optimized structures, the repulsion between the atoms in the same dimer is dominant for X=H, while that between the atoms in adjacent dimers is significant for X=I. The latter is responsible for the $c(4 \times 2)$ structure observed for I/Si(100) at a coverage of 0.5 ML, where monoiodide dimers and vacant dimers alternate with each other [91]. (There should also be a significant repulsion between the iodine atoms adjacent along the dimer row direction, which are 3.84 Å apart from each other.)

4.3.2 Desorption energy of adsorbates

The desorption energies of the X_2 molecules, E_{mol} , are shown in Table 4.2. They were calculated by subtracting the total energies of the adsorbed systems from the sum of those for the clean surface (composed of buckled dimers) and the free molecules. An ab initio calculation by de Wijs et al. for Cl/Si(100) yielded 5.3 eV for E_{mol} , in close agreement with our results [87]. Using the experimental values for the dissociation energies of the gaseous X_2 molecules [98], which are 4.8, 2.5, 2.0 and 1.6 eV for H_2 , Cl_2 , Br_2 and I_2 , respectively, the desorption energies of the X atoms (i.e., the Si-X bond energies), E_{atom} , can be estimated from E_{mol} and are also displayed in Table 4.2. It should be noted that E_{atom} obtained with the above procedure might

be underestimated slightly as compared to their counterparts that would be obtained using the total energies for the free atoms calculated with the DFT-LDA scheme, since it is known to overestimate dissociation energies of molecules in general compared to experiments. It is expected from Table 4.2 that desorption of H_2 molecules and I atoms can take place relatively easily. In fact, thermal desorption studies for H/Si(100) [20, 21] and I/Si(100) [18] showed that H_2 and I are the dominant desorption products, respectively. For Cl/Si(100), the amount of the desorbed Cl atoms was observed to be small [15] or negligible [17, 16], $SiCl_2$ being the dominant product. For Br/Si(100), Jackman et al. reported the desorption of Br atoms [18], while Flowers et al. found no evidence of it and concluded that all the adsorbed Br atoms desorb as $SiBr_2$ [19]. These observations are qualitatively consistent with the desorption energies shown in Table 4.2 in that the bond strengths of the Si-X bonds are in the order of Si-Cl > Si-Br > Si-I. More thorough discussions will be given in Sec. 4.6.

4.4 3×1 surfaces

In this section, we discuss the X/Si(100) 3×1 surfaces (with X=H, Cl or Br) consisting of alternating monohalide (monohydride) dimer units and dihalide (dihydride) units, as shown in Fig. 4.1(b). Calculations were performed with the 3×1 unit cell and $4/3$ ML of the adsorbates. We have not performed such calculations for I/Si(100), since the 3×1 surface seems unrealistic due to the substantial interatomic repulsion between the adsorbed iodine atoms.

4.4.1 Surface structure

As a result of the optimizations of the atomic configurations, both the $(SiX)_2$ and SiX_2 units were found to be symmetric for all the kinds of the adsorbates. Tables 4.3 and 4.4 display several structural parameters characterizing the optimized structures, the definitions of which are shown in Fig. 4.5. For X=H, the angle between the Si-Si dimer bond and an Si-H bond in

X	c [Å]	χ [deg.]	d [Å]	a [Å]
H	1.54	110.9	2.41	2.35
Cl	2.09	98.8	2.39	2.36
Br	2.30	98.5	2.40	2.37

Table 4.3: The values of some structural parameters characterizing the monohalide (or monohydride) dimer unit for the optimized structure of the X/Si(100) 3×1 surface with a coverage of $4/3$ ML. For the definitions of the parameters, see Fig. 4.5.

X	b [Å]	α [deg.]	β [deg.]
H	2.34	108.5	110.5
Cl	2.30	103.0	112.9
Br	2.28	98.7	114.4

Table 4.4: The values of some structural parameters characterizing the dihalide (or dihydride) unit for the optimized structure of the X/Si(100) 3×1 surface with a coverage of $4/3$ ML. For the definitions of the parameters, see Fig. 4.5.

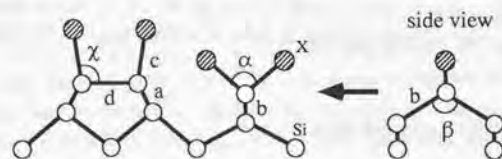


Figure 4.5: The definitions of several structural parameters characterizing the X/Si(100) 3×1 surface. Its side view is also shown. Note that the SiX_2 unit is bonded to the substrate with two Si-Si backbonds.

a dimer unit, χ , is almost identical to that for the 2×1 monohydride surface (which is close to the tetrahedral angle of 109.5°), while the directions of the Si-X bonds approach the surface normal in the cases of X=Cl and Br with χ equal to 99° and 98° , respectively. These results clearly show that the structures of the 3×1 surfaces for X=Cl and Br are highly strained. As mentioned in the previous section, the Coulomb repulsion between the adsorbates does not alter the surface structure significantly in the case of the 2×1 monohalide (or monohydride) surfaces with a coverage of 1 ML. However, at the 3×1 surfaces with a larger coverage of $4/3$ ML, such a repulsive interaction becomes so appreciable as to significantly distort the surface structures for X=Br and Cl. In contrast, as H is very small in atomic size, the interatomic repulsion between the neighboring hydrogens in adjacent monohydride and dihydride units is negligible even for the 3×1 surface, and such a repulsive interaction manifests itself only when the H/Si(100) 1×1 structure with an even larger coverage of 2 ML is formed, where the structure involving canted dihydride units (Fig. 4.1(d)) becomes energetically favorable, as was shown by Northrup [80].

The strain of the surface structures found for the halogen-adsorbed surfaces can also be seen from the Si-Si backbonds of the (silicon) dihalide units. The lengths of the backbonds, b , are 2.30 and 2.28 Å and the angles between the two backbonds that bind a dihalide unit to the surface, β , are 112.9° and 114.4° for X=Cl and Br, respectively. On the other hand, the corresponding structural parameters for X=H are 2.34 Å and 110.5° , and they are quite similar to those for crystalline Si, which are 2.35 Å and 109.5° . The contraction of the backbonds seen for the halogen adsorption is not because they become strengthened but because the dihalide units are pushed toward the surface due to the interatomic repulsion between the adsorbates. In fact, it will be shown below that the desorption energies of the units are reduced for X=Cl and Br as compared to that for X=H.

X	H	Cl	Br
Δ [eV/6×1 unit cell]	0.50	2.43	-0.04

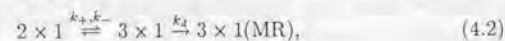
Table 4.5: The calculated values of the energy differences Δ between the X/Si(100) 3×1 and 2×1 surfaces per 6×1 unit cell. For the definition of Δ , see Eq. (4.1).

4.4.2 Stability of the 3×1 surface and estimation of the surface strain energy

For estimating how stably the X/Si(100) 3×1 surface can exist compared to the 2×1 monohalide (or monohydride) surface, a chemical potential of the atom X should be introduced as a parameter because the number of the adsorbate atoms is different for these two surfaces. Here we simply take it to be the chemical potential for which X₂ molecules can be formed from a reservoir of X atoms with no cost in energy. Then the energy difference between the 3×1 and 2×1 surfaces, Δ , is expressed as

$$\Delta = E(2 \times 1) + E(X_2) - E(3 \times 1), \quad (4.1)$$

where $E(3 \times 1)$ and $E(2 \times 1)$ are the total energies of the 3×1 and 2×1 surfaces per 6×1 unit cell, respectively, and $E(X_2)$ is the total energy of an X₂ molecule. The calculated values for Δ are displayed in Table 4.5. The negative Δ for X=Br implies that the Br/Si(100) 3×1 surface is only a metastable state. (We made it sure by a calculation with the 6×1 unit cell that the 3×1 surface is a stable structure corresponding to a local minimum of the total energy as a function of the atomic positions, and does not spontaneously transform to the 2×1 surface.) This might be related to the experimental observation that the 3×1 ordered missing row structure for Br/Si(100) is found only after the surface is annealed to high temperatures of 850-900 K [95]. The formation of the missing row structure (designated as "3×1(MR)") can be envisaged as follows:



where k_+ , k_- and k_d are the rate constants of the corresponding transformations. k_d is determined from the desorption energy of SiBr₂, which is small (about 1-2 eV), as will be shown below. The activation barrier for the transformation from the 2×1 to the 3×1 surface, which determines k_+ , is expected to be large, not only because the transformation involves extensive rearrangements of bonds between substrate Si atoms but also because the 3×1 surface is greatly destabilized by the interatomic repulsion between the adsorbed Br atoms as is apparent from the negative Δ . Therefore the barrier can be surmounted only at high temperatures. Once the 3×1 surface (with SiBr₂ units on it) is formed, however, the desorption of SiBr₂ readily takes place and then the missing row structure is stabilized due to the little chance of transforming back to the 2×1 surface.

Δ presented in Table 4.5 can be considered to be determined by the following three contributions: (1) the net energy gain E_{bond} involved in the cleavage of one X-X bond and the formation of two Si-X bonds, (2) the energy loss E_{rep} due to the interatomic repulsion between the adsorbates and the resultant surface strain, and (3) the energy E_{arr} required to rearrange substrate Si atoms from the 2×1 to the 3×1 configuration, i.e.,

$$\Delta = E_{\text{bond}} - E_{\text{rep}} - E_{\text{arr}}. \quad (4.3)$$

E_{bond} can be taken to be equal to E_{mol} shown in Table 4.2 for the monohalide (or monohydride) surfaces. Assuming $E_{\text{rep}} = 0$ for X=H, E_{arr} is estimated to be 1.69 eV, which can be reasonably taken to be independent of the kind of the adsorbates. Then one can estimate E_{rep} for X=Cl and Br to be 1.23 and 2.93 eV per 6×1 unit cell or 0.62 and 1.47 eV per 3×1 unit cell, respectively.

4.4.3 Desorption energy of SiX₂ units

The desorption energies E_{des} of the SiX₂ units are presented in Table 4.6. E_{des} was simply defined to be the energy difference between those optimized structures before and after the desorption that were obtained by calculations with the 3×1 unit cell. Actually, if a row of SiX₂ units along the dimer

X		H	Cl	Br
E_{des}	[eV]	5.03	3.11	2.31
D	[eV]	0.27	2.19	2.99
D_{rep}	[eV]	0	0.62	1.47
D_{other}	[eV]	0.27	1.57	1.52

Table 4.6: The desorption energies E_{des} of the SiX_2 units at the X/Si(100) 3×1 surfaces. Also shown are the differences D between E_{bulk} and E_{des} , where E_{bulk} is the bond energy per 2 Si-Si bonds of bulk Si, which is 5.3 eV. D_{rep} and D_{other} are the contributions to D from the interatomic repulsion between the adsorbates and the other effects, respectively.

row direction are desorbed, the substrate Si atoms to which those SiX_2 units are bonded are exposed and are expected to form dimers in the direction perpendicular to that of the surface dimers, as schematically illustrated in Fig. 4.6. Such a situation is expected to be realized in the 3×1 ordered missing row structure observed for Br/Si(100). The use of the 3×1 unit cell in the calculations, however, prohibited such dimer formation.

Thus we also performed calculations for Br/Si(100) with the 3×2 unit cell, where a set of 4 k points were employed to make the calculations tractable. We considered three kinds of the 3×2 surfaces, which contain m SiBr_2 units per 3×2 unit cell with $m = 0, 1$ and 2. The total energies for the three surfaces, which are denoted by E_0 , E_1 and E_2 , were calculated. The surface with $m = 2$ has actually the 3×1 periodicity. We can then obtain the desorption energies of an SiBr_2 unit in the presence and absence of SiBr_2 units adjacent to it, which are denoted by E_p and E_a , respectively. E_p is given by $E_1 + E(\text{SiBr}_2) - E_2$, while E_a is expressed as $E_0 + E(\text{SiBr}_2) - E_1$, where $E(\text{SiBr}_2)$ represents the total energy of an isolated SiBr_2 molecule. E_p and E_a are calculated to be 2.1 and 0.9 eV, respectively. Thus the rate-limiting step is the desorption of an SiBr_2 unit with its neighboring units present, and once such a unit is desorbed, the desorption of one of its adjacent units is expected to take place relatively easily. The nominal value for the activation

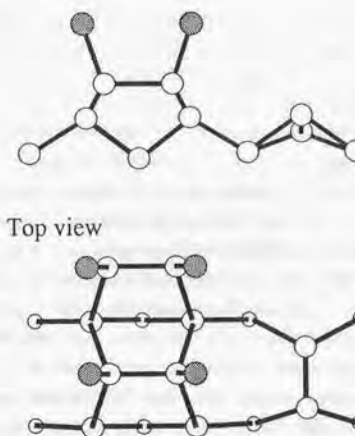


Figure 4.6: A 3×2 surface which can be considered to correspond to the 3×1 ordered missing row structure observed for Br/Si(100).

energy of the thermal desorption of SiBr_2 from $\text{Br}/\text{Si}(100)$ was experimentally determined to be 1.9 eV [18] in good agreement with the above value of 2.1 eV. It is not evident, however, whether such a direct comparison can be made, because the desorption is quite a complicated process and what determines the activation energy is obscure. The sum of E_p and E_a differs from $2E_{\text{des}}$ by 1.6 eV, which corresponds to the energy gain through the dimer formation upon the desorption of the SiBr_2 units as described above.

E_{des} presented in Table 4.6 can be considered to represent the energy loss as a direct consequence of the removal of an SiX_2 unit from the surface and does not include indirect effects such as the energy gain through the dimer formation. Since an SiX_2 unit is bonded with two Si-Si backbonds to the substrate and its desorption involves the cleavages of these bonds, it is interesting to compare E_{des} with twice the Si-Si bond energy. The latter can be estimated from the cohesive energy E_{bulk} of bulk Si, which is calculated to be 5.3 eV/atom (or eV per two Si-Si bonds) with the LDA [99]. (Note that the LDA tends to overestimate Si-Si bond energies, as can be seen from the fact that the experimental value of the cohesive energy is 4.6 eV/atom. It is quite likely that such overestimation is involved in the desorption energies of the SiX_2 units shown in Table 4.6 and those that will be presented in Table 4.7. It is still meaningful, however, to compare Si-Si bond energies in various environments obtained with the same calculational scheme, that is, the LDA in the present case.) The difference D between E_{bulk} and E_{des} is also displayed in Table 4.6. The comparisons suggest that the desorption of SiX_2 is facilitated remarkably by the presence of the halogen adsorbates, while the hydrogen adsorption affects the strength of the backbonds only slightly. These results are quite consistent with the fact that the hydrogen-adsorbed 3×1 surface shown in Fig. 4.1(b) is stable and etching processes do not proceed efficiently, whereas in the case of Br adsorption 3×1 domains with missing rows are observed experimentally instead of such a surface structure as seen for $\text{H}/\text{Si}(100)$.

It is apparent that the interatomic repulsions between the halogen adsorbates destabilize the 3×1 surfaces, which are the initial states of the desorp-

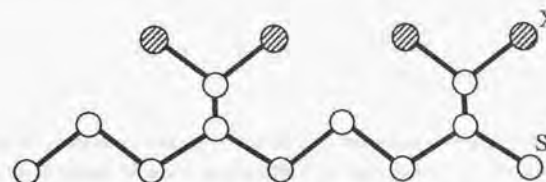


Figure 4.7: The atomic structure of the strain-free 2×1 surface with SiX_2 units.

tion processes, thus lowering the desorption energies for $\text{X}=\text{Cl}$ and Br . The reductions D_{rep} in the desorption energies due to the repulsions can be taken to be equal to E_{rep} estimated in the previous subsection, which are 0.62 and 1.47 eV per 3×1 unit cell for $\text{X}=\text{Cl}$ and Br , respectively. These large values clearly indicate that such strain (and interatomic repulsion responsible for it) as seen in the 3×1 surfaces plays a crucial role in weakening surface bonds, thus promoting, e.g., etching processes. The subtractions of D_{rep} from D shown in Table 4.6 yield the decreases D_{other} of the desorption energies that can be ascribed to the other effects than the interatomic repulsions, which are 0.27, 1.57 and 1.52 eV for $\text{X}=\text{H}$, Cl and Br , respectively. The values of D_{other} are summarized in Table 4.6 along with D_{rep} . What gives rise to D_{other} will be discussed in subsequent sections.

4.5 Strain-free 2×1 surfaces with SiX_2 units

In order to address the question as to whether the desorption energies of the SiX_2 units are actually diminished or not by the presence of the halogen adsorbates even without the interatomic repulsion between the adsorbates and the resultant surface strain, we performed calculations with the 2×1 unit cell for those model surfaces with SiX_2 units which are free of strain as shown in Fig. 4.7. This surface structure is similar to that proposed by de

X		H	Cl	Br	I
E'_{des}	[eV]	4.90	3.71	3.76	3.82
D'	[eV]	0.40	1.59	1.54	1.48
n		2.1	3.0	2.8	2.5

Table 4.7: The desorption energies E'_{des} of the SiX_2 units at the X/Si(100) 2×1 model strain-free surfaces (Fig. 4.7). The differences D' between E'_{bulk} and E'_{des} , where E'_{bulk} is the bond energy per 2 Si-Si bonds of bulk Si ($=5.3$ eV), are presented as well as the electronegativities n of the adsorbate elements.

Wijs et al. as a possible intermediate state of the thermal desorption process of SiCl_2 from the Cl/Si(100) 2×1 monochloride surface [96]. They considered that such a structure is formed via the monochloride-dichloride isomerization reaction (see Fig. 4.3) followed by the diffusion of the Si atom that has lost the Cl atom. Without such a diffusion, a dichloride species once produced would transform back to a monochloride one before the desorption of the dichloride. The calculated desorption energies of the SiX_2 units are displayed in Table 4.7. The differences D' between E'_{des} and E'_{bulk} ($=5.3$ eV) are also shown in Table 4.7. It is important to note that even on the strain-free surfaces the desorption energies for X=Cl, Br and I are appreciably diminished compared with that for X=H. And more importantly, the values of D' are almost equal to D_{other} in Table 4.6 within an error of about 0.1 eV for X=H, Cl and Br. The latter represent the reductions in the desorption energies (relative to the bulk Si-Si bond strength per two bonds) at the 3×1 surfaces, with the effect of the interatomic repulsions subtracted. Therefore D' (and also D_{other}) can be regarded as quantities that are inherent to the adsorbate atoms themselves and are universal in the sense that they do not depend on the environments of Si surfaces upon which the atoms are adsorbed.

One of the typical quantities characterizing atoms is Pauling's electronegativity [100], which is also shown for each adsorbate in Table 4.7. D' can be seen to follow closely the trends of the electronegativities. Since electroneg-

activities characterize atoms by their ability to attract electrons, it might be reasonable to consider that the electronegative halogen adsorbates tend to pull significant bond charge out of the Si-Si backbonds associated with the SiX_2 units, whereby reducing their desorption energies. Such an effect is then expected to be small for the adsorption of hydrogen, since its electronegativity ($=2.1$) is close to that of Si ($=1.8$). Figure 4.8 displays contour plots for the total charge density at the plane including the two Si-Si backbonds that bind an SiX_2 unit to the substrate for X=H and Br. One can clearly see that the bond charge of those backbonds is *polarized* for X=Br, while it is not for X=H. It is unclear, however, whether the bond charge is *diminished* or not by the adsorption of Br (and the other halogens under consideration) as compared to that in the case of the adsorption of H. This point will be addressed in Sec. 4.7.

There have been few studies that have discussed weakenings of Si-Si backbonds in the presence of electronegative halogen adsorbates quantitatively, though they play quite an essential role in determining the efficiencies of a variety of etching processes. Thus the systematic data of D' (or E'_{des}) presented in Table 4.7 are expected to be of great use in achieving a comprehensive understanding of etching processes of Si surfaces with halogen gas. In the following section, we interpret the available data of thermal desorption experiments for the X/Si(100) surfaces (X=H, Cl, Br or I) in terms of E'_{des} with the interatomic repulsions that can manifest themselves at high-coverage surfaces taken into account.

4.6 Interpretation of experiments

Table 4.8 shows again the desorption energies of the X atoms, $E(X)$ ($\equiv E_{\text{atom}}$ in Table 4.2), those of the X_2 molecules, $E(\text{X}_2)$ ($\equiv E_{\text{mol}}$ in Table 4.2), and those of the SiX_2 units, $E(\text{SiX}_2)$ ($\equiv E'_{\text{des}}$ in Table 4.7), in the absence of the interatomic repulsions between the adsorbates. We also show in Table 4.8 the dominant products observed in thermal desorption studies of the X/Si(100) surfaces [20, 21, 15, 17, 16, 18, 19]. Comparisons among

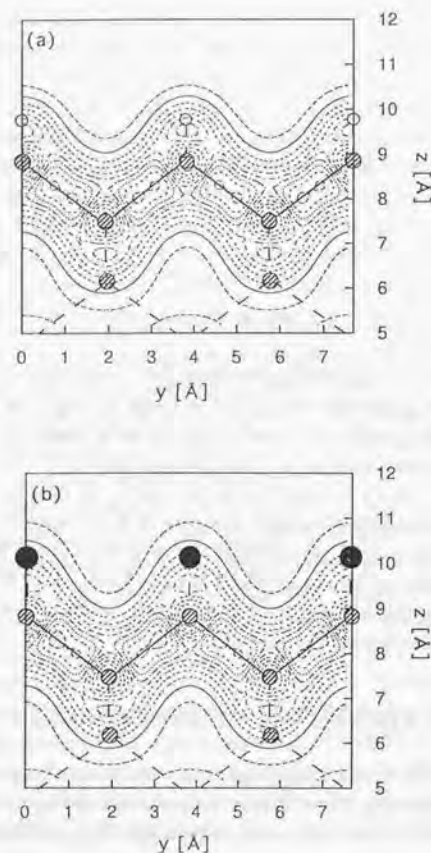


Figure 4.8: Contour plots for the total charge density at the plane including the two Si-Si backbones associated with an SiX_2 unit at the $\text{X/Si}(100)$ 2×1 model strain-free surfaces with (a) $\text{X}=\text{H}$ and (b) $\text{X}=\text{Br}$. The open, solid and hatched circles represent H, Br and Si atoms, respectively.

X	$E(\text{X})$	$E(\text{X}_2)$	$E(\text{SiX}_2)$	exp.
H	3.5	2.19	4.90	H_2
Cl	3.9	5.35	3.71	SiCl_2
Br	3.3	4.58	3.76	SiBr_2 , Br
I	2.6	3.62	3.82	I

Table 4.8: The desorption energies of the X atoms, $E(\text{X})$, those of the X_2 molecules, $E(\text{X}_2)$, and those of the SiX_2 units, $E(\text{SiX}_2)$, in the absence of the interatomic repulsions between the adsorbates (in units of eV). Also shown in the column designated as "exp." are the dominant products experimentally observed in thermal desorption studies for the $\text{X/Si}(100)$ surfaces.

$E(\text{X})$, $E(\text{X}_2)$ and $E(\text{SiX}_2)$ suggest that H_2 , SiCl_2 , Br and I are most easily desorbed for each of the adsorbates, in good agreement with the experiments. It should be noted that $D(\text{X})$ would be slightly larger than those presented in Table 4.8 if they were obtained from calculations alone, as mentioned in Sec. 4.3.

For $\text{Br/Si}(100)$, Jackman et al. reported the desorption of both Br atoms and SiBr_2 molecules, with the ratio of the latter to the former increasing with increasing Br coverage [18]. As the coverage of the adsorbates increases, the interatomic repulsions between the adsorbates are expected to become significant especially for such large adsorbates as Br and to appreciably lower the desorption energies of SiBr_2 units in a region with a locally high concentration of the adsorbates. Though the desorption energies of some Br atoms are also expected to be diminished by the repulsions, the lowerings of the desorption energies of the SiBr_2 units are more appreciable as the desorption of an SiBr_2 unit in such a region can lead to a larger decrease in the repulsion energy (as well as a more extensive relaxation of the surface strain which has been induced by the repulsions) than that of a single Br atom in the same region. Considering that the repulsion energy calculated for the $\text{Br/Si}(100)$ 3×1 surface is as large as 1.47 eV (Table 4.6), such a repulsion effect can be large enough to make the desorption of SiBr_2 preferable to that of Br at

high-coverage surfaces, in accord with the above experimental observation by Jackman and co-workers. Thus we consider that such an effect originated in the interatomic repulsions between adsorbates is one of the most important factors that determine the efficiencies of various etching processes.

This can also be seen from the following observation. The peak temperatures in the observed thermal desorption spectra (TDS) for the Br/Si(100) [18] and Cl/Si(100) [15] surfaces are 770 and 900 K with heating rates of 50 K/s and 5 K/s, respectively, illustrating that SiBr₂ is more readily desorbed than SiCl₂. Since the calculated desorption energy of SiBr₂ is slightly larger than that of SiCl₂ in the absence of the interatomic repulsions between the adsorbates (Table 4.8), the difference observed in the TDS can also be considered to be derived from such a repulsion effect as described above. That is, the desorption occurs preferentially in a region with a high local concentration of the adsorbates, where the interatomic repulsions between the adsorbates promote the desorption of SiBr₂ more significantly than that of SiCl₂, since Br is larger in atomic size than Cl.

Adsorption of hydrogen does not induce etching, not only because it results in only a slight weakening of the backbonds intrinsically (as can be seen from small D' in Table 4.7), but also because it does not induce such a repulsion effect as described above due to its small atomic size. Table 4.7 shows that the backbonds are weakened by adsorption of iodines almost as much as in the case of Cl or Br adsorption. Thus the fact that adsorption of iodines does not result in efficient etching can be attributed to the weakness of the Si-I bonds. Since the degrees of the weakenings of the backbonds seem to roughly follow the trends of the electronegativity as has been argued in the previous section, adsorption of fluorines, whose electronegativity is 4.0, is expected to weaken the backbonds even more significantly than that of Cl, thus promoting etching more efficiently. Note that Si-F bonds are known to be much stronger than Si-Cl bonds.

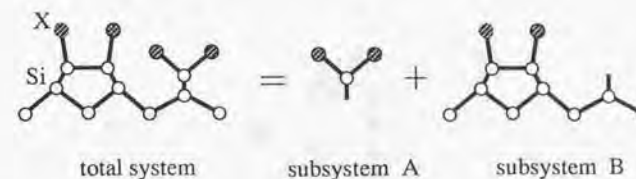


Figure 4.9: Schematic illustration of how the X/Si(100) 3×1 surface is divided into two subsystems A and B in performing a population analysis in the way described in Subsec. 2.2.3.

4.7 Population analysis

In this section, we present and discuss the results of the population analyses performed by means of the scheme described in Subsec. 2.2.3 to address the important question as to why the adsorption of the halogen atoms weakens the Si-Si backbonds significantly as shown in Table 4.7. We first applied the population analysis scheme to the 3×1 surfaces. The total system was divided into subsystems A and B in the way illustrated in Fig. 4.9 to investigate properties of the Si-Si backbonds associated with the SiX₂ units. N_A and N_B were taken to be equal to the numbers of the basis functions that would be used in calculations for the subsystems with minimal basis sets of the LCAO type, i.e., 4 (1 for 2s and 3 for 2p) per Si or Cl atom, 4 (1 for 3s and 3 for 3p) per Br atom, and 1 (for 1s) per H atom in the unit cell. The calculated total overlap populations, p , are presented in Table 4.9 together with the desorption energies of SiX₂. It can be seen that the total overlap populations reproduce the trends of the desorption energies well. Figure 4.10 displays the COOP curves for X=H and Br. The COOP curve for X=Cl (not shown) is basically similar to that for X=Br. The integrals of the COOP curves up to the Fermi level are equal to the total overlap populations. As is apparent from Fig. 4.10, the COOP curve for X=Br exhibits marked negative contri-

X	p	E_{des}
H	1.36	5.03
Cl	1.06	3.11
Br	0.92	2.31

Table 4.9: The total overlap populations, p , are presented together with the desorption energies of SiX_2 , E_{des} , calculated for the X/Si(100) 3×1 surfaces.

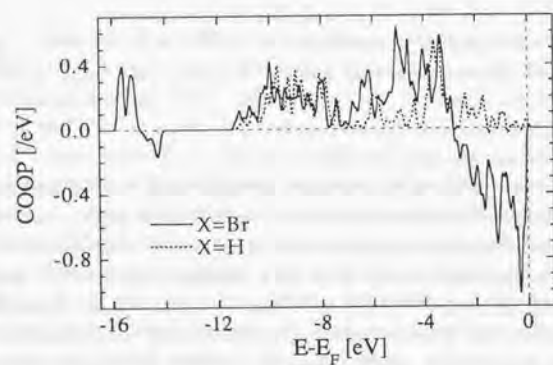


Figure 4.10: The COOP curves with respect to the bonding between the SiX_2 unit and the rest of the system at the X/Si(100) 3×1 surfaces with X=H (dotted line) and X=Br (solid line).

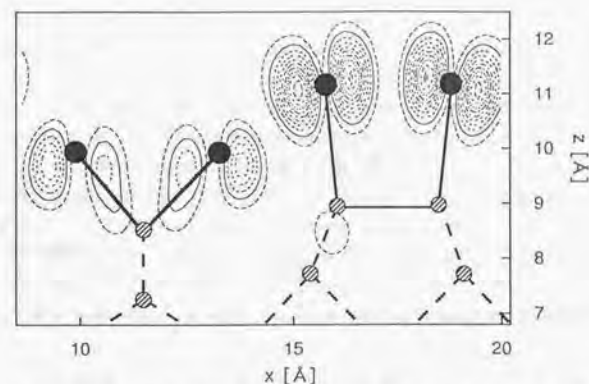


Figure 4.11: A contour plot for the charge density of the orbital in the highest occupied band with $\mathbf{k} = \Gamma$ at the plane including the SiX_2 units. The solid and hatched circles represent Br and Si atoms, respectively.

Contributions ranging from -3 to 0 eV relative to the Fermi level. However, these contributions do not necessarily indicate that the orbitals giving rise to them have anti-bonding character with respect to the Si-Si backbones. Figure 4.11 displays a contour plot for the charge density distribution at the plane including the SiX_2 units for the orbital in the highest occupied band with $\mathbf{k} = \Gamma$, which has a large negative overlap population. Another charge density plot (not shown) for this orbital at the plane including the Si-Si backbones exhibits almost no charge around them, ruling out the possibility that the orbital has anything to do with them. It is then apparent from Fig. 4.11 that the large negative overlap population of the orbital stems from anti-bonding character due to the interactions between electronic levels (2p lone pairs) of a Br atom in the SiBr_2 monomer and the neighboring Br atom in the SiBr dimer. There should also be bonding orbitals resulting from the interactions, which are considered to be responsible for the significantly enhanced bonding contributions from -7 to -4 eV (relative to the Fermi level) seen in the COOP

curve for X=Br in Fig. 4.10 as compared to those for X=H. According to the simple molecular orbital theory, two fully occupied electronic levels interact to result in a net anti-bonding contribution (that enhances as the overlap integral between the levels gets larger). Therefore the interaction between electronic levels of the adsorbed Br atoms is considered to be at least partly responsible for the diminished value of the total overlap population p for X=Br as compared to that for X=H (see Table 4.9), and the same goes for X=Cl. In this way effects that are irrelevant to any covalent bonds but that affect a desorption energy can be partly incorporated in the corresponding total overlap population, whereby achieving a strong correlation between the desorption energy and the total overlap population as can be seen from Table 4.9.

The COOP curve for X=H shown in Fig. 4.10 exhibits almost no such negative contributions as seen for X=Br (and Cl), indicating that there is almost no (repulsive) interaction between the electronic levels of the adsorbates. Note that the COOP curve would consist only of positive contributions below the Fermi level if it were not for any effects incurred by the presence of any adsorbates, since every state in the valence bands of, say, pure crystalline Si has bonding character with respect to the Si-Si bonds.

As described above, the total overlap populations calculated by dividing the system in the way illustrated in Fig. 4.9 contain the contributions from the repulsive interactions between the adsorbates in addition to those corresponding to the bond charges of the Si-Si backbonds associated with the SiX₂ units. Aiming at separating these two contributions, we performed population analyses by dividing the total system (i.e., the 3×1 surface) into three subsystems, namely, the SiX₂ monomer (subsystem A), the SiX dimer (subsystem B), and the rest of the substrate (subsystem C), as illustrated in Fig. 4.12. The total overlap populations between the subsystems A and B, A and C, and B and C are denoted by $p(A-B)$, $p(A-C)$, and $p(B-C)$, respectively, and are listed in Table 4.10. The negative values for $p(A-B)$ indicate the repulsive interactions between the adsorbates, which are almost negligible for X=H but substantial for X=Cl and Br, as expected. $p(A-C)$ and $p(B-C)$

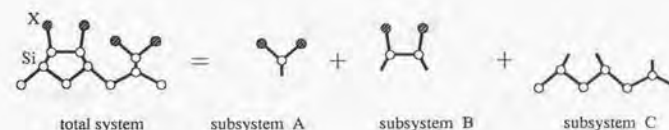


Figure 4.12: Schematic illustration of how the X/Si(100) 3×1 surface is divided into three subsystems A, B and C in performing a population analysis in the way described in Subsec. 2.2.3.

X	$p(A-B)$	$p(A-C)$	$p(B-C)$
H	-0.03	1.30	2.60
Cl	-0.25	1.22	2.63
Br	-0.31	1.09	2.57

Table 4.10: The total overlap populations between the subsystems A and B, A and C, and B and C, denoted by $p(A-B)$, $p(A-C)$, and $p(B-C)$. For the definitions of the subsystems A, B and C, see Fig. 4.12.

X	p'	E'_{des}
H	1.34	4.90
Cl	1.23	3.71
Br	1.17	3.76
I	1.13	3.82

Table 4.11: The total overlap populations, p' , and the desorption energies of SiX_2 , E'_{des} , calculated for the X/Si(100) 2×1 strain-free surfaces.

correspond to the bond charge of the 2 backbonds of the SiX_2 monomer and that of the 4 backbonds of the SiX dimer, respectively. For X=H, $p(\text{B-C})$ is almost exactly twice as large as $p(\text{A-C})$, indicating that the strengths of the two kinds of the backbonds are almost identical. As the adsorbates are varied from H to Cl and Br, $p(\text{B-C})$ remains almost constant, while $p(\text{A-C})$ is appreciably reduced, indicating that the backbonds associated with the SiX_2 monomer are more significantly influenced by the adsorbates than those of the SiX dimer. It should be noted, however, that the sum of $p(\text{A-B})$ and $p(\text{A-C})$ deviates a little from p given in Table 4.9 for each adsorbate, though it should not in principle. Since larger errors in the expansions of the wavefunctions as shown in Eq. (2.20) were found to arise in the present population analyses than in those performed in the way described in Fig. 4.9, the data given in Table 4.10 are considered to be less reliable than those in Table 4.9. It seems that in performing population analyses the total system should be divided into as few subsystems as possible. We discuss below only the results of the population analyses in which the total system was divided into two subsystems, i.e., the SiX_2 unit and the rest of the system.

We then performed population analyses for the 2×1 strain-free surfaces, which do not involve the interatomic repulsions between the adsorbates. The calculated total overlap populations, p' , are displayed in Table 4.11 along with the desorption energies of SiX_2 . It can be seen that the total overlap populations for the halogens are significantly smaller than that for hydrogen.

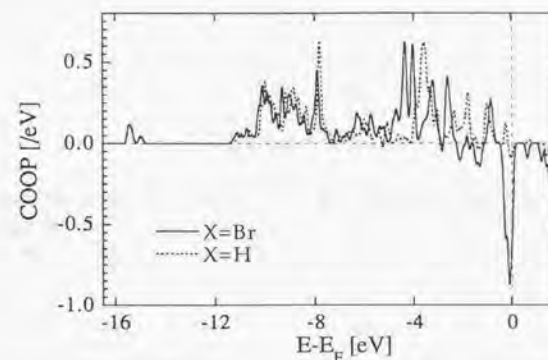


Figure 4.13: The COOP curves with respect to the bonding between the SiX_2 unit and the rest of the substrate at the X/Si(100) 2×1 strain-free surfaces with X=H (dotted line) and X=Br (solid line).

The COOP curves for X=H and Br are shown in Fig. 4.13. The COOP curve for X=Br (and also those for X=Cl and I, though not shown) exhibits large negative contributions just below the Fermi level, which are almost absent in the case of X=H. Therefore it might first appear that the orbitals yielding these negative contributions are responsible for the substantial reduction in the total overlap populations seen for the halogens. By examining the charge density distribution of the orbitals, it was found that they are derived from the Si dangling bonds present at the surfaces, and their anti-bonding character is considered to result from the interactions of the dangling bonds with the adsorbates. However, the molecular orbital theory ensures that the corresponding bonding orbitals should be present lower in energy.

In order to determine whether such interactions affect the total overlap populations substantially or not, we performed total energy calculations and population analyses for X/Si(100) 2×1 surfaces that are identical to the sur-

X	p''	E''_{des}
H	1.35	4.89
Cl	1.22	3.76
Br	1.12	3.65
I	0.96	2.49

Table 4.12: The total overlap populations, p'' , and the desorption energies of SiX_2 , E''_{des} , calculated for X/Si(100) 2×1 surfaces that are identical to the surfaces as shown in Fig. 4.7 except in that the Si dangling bonds are terminated by hydrogens.

faces discussed above (shown in Fig. 4.7) except in that the Si dangling bonds present at the latter surfaces are terminated by hydrogens. The calculated desorption energies and the total overlap populations are presented in Table 4.12. As is apparent from Tables 4.11 and 4.12, the total overlap populations are almost identical for X=Cl (and also for X=H) irrespective of whether the dangling bonds are terminated by hydrogens or not, which rules out the possibility that the interactions between the dangling bonds and the adsorbates contribute much to the reduction in the total overlap populations seen for the halogens. (Note that for X=Br and I the repulsive interactions between orbitals of the adsorbates and ones of the terminating hydrogens become appreciable, as can be seen from the smaller desorption energies compared to those for the surfaces without the terminating hydrogens, and diminish the total overlap populations.) Therefore we can safely interpret the total overlap populations shown in Table 4.11 as the bond charges of the Si-Si backbonds and conclude that the bond charges are substantially diminished by the adsorption of the halogens as compared to that in the case of the hydrogen adsorption.

The total overlap populations shown in Table 4.11 are, however, somewhat inconsistent with the trends of the desorption energies and the electronegativities for the halogens. This might be attributed to an overestimation of the absolute values of the (negative) overlap populations for the

anti-bonding orbitals derived from the dangling bonds. Such an overestimation is often seen in the Mulliken population analysis especially for unoccupied states (see, e.g., Fig. 2.1), and might be seen also for partially occupied states such as the dangling bond states. As the atomic sizes of the adsorbates increase from Cl to I, the overestimation is expected to become more pronounced and to result in larger errors in the total overlap populations.

We then discuss the relation between a desorption energy and the corresponding total overlap population. The total energy of a system, E_{tot} , can be expressed as a sum of the electron-electron, electron-ion and ion-ion interaction energies (denoted by E_{ee} , E_{ei} and E_{ii} , respectively) as

$$E_{tot} = E_{ee} + E_{ei} + E_{ii}. \quad (4.4)$$

When a many-electron problem is reduced to a one-electron problem by treating the electron-electron interactions in a mean-field manner, one obtains the one-electron energies $\{\epsilon_\mu\}$ and the sum of them over all the occupied one-electron orbitals, E_{oe} , is equal to $2E_{ee} + E_{ei}$ due to the double countings of the electron-electron interactions. We then obtain the following expression for the total energy [101]:

$$E_{tot} = E_{oe} + (E_{ii} - E_{ee}). \quad (4.5)$$

The desorption energy of a unit, E_d , is defined as the difference between the total energies before and after its desorption, which can be decomposed into the differences of the above three terms as

$$E_d = \Delta E_{oe} + (\Delta E_{ii} - \Delta E_{ee}). \quad (4.6)$$

The total overlap population has been shown to be roughly proportional to ΔE_{oe} [4], while the second and third terms in the right hand side of Eq. (4.6) cannot usually be neglected. Figure 4.14 displays the relation between the desorption energies of the SiX_2 units and the corresponding total overlap populations presented above for the 3×1 surfaces, the strain-free 2×1 surfaces (with dangling bonds), and the 2×1 surfaces with dangling bonds terminated

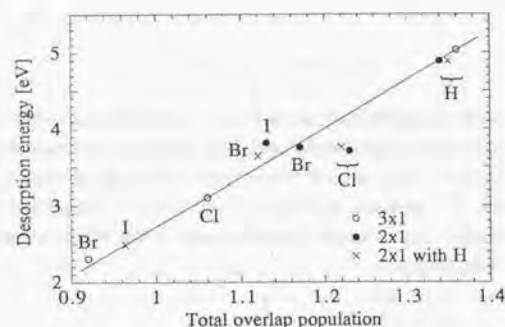


Figure 4.14: The relation between the desorption energies and the total overlap populations associated with the SiX_2 units for the 3×1 surfaces (open circles), the strain-free 2×1 surfaces (solid circles), and the 2×1 surfaces with dangling bonds terminated by hydrogens (crosses). The solid line is a guide to the eyes.

by hydrogens, where a strong correlation between them can be clearly seen. It can be seen from Fig. 4.14 that the overlap populations reproduce all the qualitative trends of the desorption energies, i.e., the diminished bond charge of the Si-Si backbonds for the halogen adsorption compared to that for the hydrogen adsorption, the interadsorbate repulsions and the repulsions between the adsorbates and the hydrogens terminating the dangling bonds. (The seemingly linear relation seen in Fig. 4.14 suggests that the second and third terms in the right hand side of Eq. (4.6) are almost independent of the type of the surfaces as well as the kind of the adsorbates, the reason for which remains to be clarified.) This clearly indicates not only that the new population analysis scheme used here works well but also that a total overlap population calculated with the scheme can serve as a rough measure of the corresponding desorption energy. It might then be possible that the COOP curve, which displays the energy-resolved contributions to the total overlap population, can provide information on what gives rise to the desorption energy, which might be of great use in gaining insights into, e.g., photo-induced etching processes.

4.8 H/Si(100) 1×1 surface

In this section we touch on the H/Si(100) 1×1 surface. As described above, adsorption of hydrogens does not weaken the Si-Si backbonds appreciably. In fact, thermal desorption from H/Si(100) surfaces yields only a small amount of silicon-containing species, even if a surface prepared with an extensive exposure to hydrogen gas, which is considered to form a 1×1 structure, is used. However, it has been observed by STM that etching takes place at the 1×1 surfaces under a *continuous* exposure to atomic hydrogen gas [76, 77]. Note that the 2×1 and 3×1 phases are stable against etching even under such a continuous exposure.

We calculated the total energies for the H/Si(100) 1×1 surfaces consisting of symmetric and canted dihydrides, which are illustrated in Figures 4.15(a) and (b), respectively. The latter has been shown to be by 0.17 eV ($\equiv \Delta_1$)

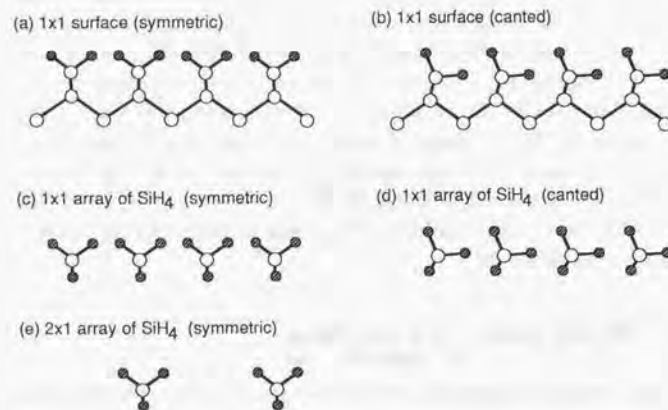


Figure 4.15: Several atomic configurations consisting of Si and H that are studied in this section in connection with the H/Si(100) 1×1 surface.

stabler than the former, in agreement with a previous calculation [80]. This energy difference can be attributed at least partly to the interatomic repulsion between the adsorbed hydrogens that is expected to be significant in the former structure. In order to estimate the repulsion energy, total energy calculations were performed for the 1×1 and 2×1 two-dimensional arrays of the symmetric SiH₄ units as shown in Fig. 4.15(c) and (e). The difference in the total energies per SiH₄ unit has been calculated to be 0.25 eV ($\equiv \Delta_2$), which can be regarded as the interatomic repulsion energy involved in the 1×1 structure with the symmetric dihydrides. Note that we performed calculations for the arrays of SiH₄ instead of those of SiH₂ because the total energies for the latter would contain extra interactions between the Si dangling bonds.

Boland claimed that the strain of the backbonds seen at the 1×1 surface with the canted dihydrides results in a reduced barrier to etching reactions with gas-phase hydrogen atoms [77]. In order to estimate the bond-strain energy of the backbonds, we have calculated the total energy for the 1×1-ordered two-dimensional array of the *canted* SiH₄ units (Fig. 4.15(d)). It has been found to be lower by 0.31 eV ($\equiv \Delta_3$) than that of the 1×1 array of the symmetric SiH₄ (Fig. 4.15(c)), with the atomic structures of both arrays optimized. It should be noted that Δ_3 is larger than Δ_2 , implying that some attractive interaction might be present between the canted SiH₂ (or SiH₄) units. It can be seen that the strain of the backbonds involved in the 1×1 surface with the canted dihydrides weakens them by 0.14 eV ($= \Delta_3 - \Delta_1$) per two bonds.

We then evaluated the bond charges of the backbonds for both the 1×1 surfaces. They are 1.37 and 1.31 for those with the symmetric and canted dihydrides, respectively, reflecting the weakening of the backbonds at the latter surface. In calculating the bond charges, the total system was divided into the 1×1 array of the SiH₂ units (subsystem A) and the rest of the substrate (subsystem B). In this case, the interatomic repulsions between the adsorbates could not contribute to the (total) overlap populations between both subsystems, which allows them to be interpreted as the bond charges

of the backbonds, in contrast to the case of the 3×1 surfaces discussed in the previous section.

4.9 Summary

In this chapter, we have studied the X/Si(100) surfaces (X=H, Cl, Br and I) by means of the DFT-LDA total energy calculations and the population analysis scheme described in Subsec. 2.2.3 in order to gain insights into etching processes taking place at these surfaces.

The 2×1 monohalide (or monohydride) surfaces with a coverage of 1 ML have been studied, and the desorption energies of the X atoms and X_2 molecules have been obtained. It has been shown that the interatomic repulsions between the adsorbates are insignificant at these low-coverage surfaces.

Thermal desorption experiments for the X/Si(100) surfaces showed that the main products are H_2 , $SiCl_2$, $SiBr_2$ and I, indicating that only the adsorption of Cl and Br promotes etching. In order to clarify the origin of such different behaviors, we have considered two types of the surfaces involving SiX_2 species on them, both of which can be intermediate states of the etching processes. One is the 3×1 surface with a coverage of $4/3$ ML which consists of alternating rows of SiX_2 monomers and SiX dimers, and the other is a 2×1 surface with a coverage of 1 ML. We have studied the cases of X=H, Cl and Br for the former and those of X=H, Cl, Br and I for the latter. It has been found that the interatomic repulsion between the adsorbates results in a highly strained structure at the former surface in the cases of X=Cl and Br (and presumably also of X=I), while the latter surface is free of such strain due to the low coverage.

We have calculated the desorption energies of SiX_2 for each type of the surfaces, and have shown those for X=Cl, Br and I to be considerably lower than those for X=H. Based on these desorption energies, it has been revealed that upon adsorption of X atoms onto the Si(100) surfaces the Si-Si backbonds that bind the SiX_2 units to the substrate are weakened by amounts that are inherent to the adsorbates themselves and that are almost indepen-

dent of the surrounding surface conditions. It has been argued that further reduction in the desorption energies can be incurred by the interatomic repulsions between the adsorbates that manifest themselves at surfaces with high coverages of large-sized adsorbates such as the Br/Si(100) 3×1 surface. We have been able to consistently explain the available experimental data on thermal desorption from the X/Si(100) surfaces by taking into account both of the above-mentioned effects leading to the reduction in the desorption energies of SiX_2 .

Since the degrees to which the backbonds are weakened appear to follow the trends of the electronegativities of the adsorbates, the picture in which electronegative adsorbates weaken the backbonds by pulling bond charge out of them has been invoked. In order to determine whether the picture is correct or not, we have evaluated the bond charge of the backbonds by means of our population analysis scheme and found that it is significantly smaller in the case of the halogen adsorption than for the hydrogen adsorption. We have also found a strong correlation between the total overlap populations (associated with the bonding between the SiX_2 and the surface) and the desorption energies of SiX_2 for all the above-mentioned surfaces, which suggests that the present population analysis scheme can be of great use in interpreting desorption energies obtained by total energy calculations.

We have also studied H/Si(100) 1×1 surfaces, on which etching has been known to occur under a continuous exposure to atomic hydrogen gas. The bond charge of the backbonds has been found to be smaller at the surface consisting of the canted dihydrides than at that of the symmetric ones. This indicates a weakening of the backbonds caused by the bond-strain at the former surface, which might facilitate an etching reaction with gas-phase atomic hydrogens.

Chapter 5

Concluding remarks

We have studied CO/Pt(111) and X/Si(100) (with X being H, Cl, Br or I), which are among the most typical chemisorption systems that are of great fundamental as well as technological importance, by means of the DFT-LDA first-principles calculations. We have addressed the following basic questions concerning chemical bonds at these surfaces: (1) How is the chemisorption bond between CO and the surface stably formed at CO/Pt(111)? (2) How does the adsorption of the different adsorbates affect the Si-Si backbonds, the cleavages of which result in etching, at X/Si(100)? Emphases have been placed on gaining chemical (and thus local) understandings of these phenomena.

While several well-established population analysis schemes such as Mulliken's analysis can be exploited to achieve chemical interpretations of results of calculations in which wavefunctions are expressed as linear combinations of atomic orbitals (LCAO), it has been hard to obtain local information from calculations with plane wave basis sets, which are becoming more and more common owing to their capability of yielding results with high accuracy. Therefore we have developed a new population analysis scheme that is basically in the spirit of Mulliken's population analysis but is applicable to wavefunctions expanded with a plane wave basis set.

Using this scheme, we have discussed the adequacy of the Blyholder model for the chemisorption of CO on transition metal surfaces, which has been

recently questioned by several studies. For that purpose the CO/Pt(111) system has been studied as an example. Though an extended Hückel calculation, which is of semi-empirical nature, suggested that the 4σ orbital also plays a role in the bonding in addition to the 5σ and 2π , our *ab initio* calculations combined with the new population analysis scheme have revealed that only the 5σ and 2π are involved in the bonding through the 5σ donation and 2π backdonation, supporting the Blyholder model. Our calculations have demonstrated the existence of one-electron states which appear to be described by the atomic orbitals of C or O better than by the molecular orbitals of CO, as was observed by a recent X-ray emission spectroscopy experiment. Although this suggests that an atomic-orbital-based model might be needed to describe such individual one-electron states, the results of our population analysis mentioned above have definitely indicated that the Blyholder model, which is a molecular-orbital-based model where only two molecular orbitals are involved, provides an accurate and at the same time simple picture to describe the chemisorption mechanism.

We have also studied the X/Si(100) surfaces with X representing H, Cl, Br or I by means of DFT-LDA total energy calculations and the new population analysis scheme. We have considered two kinds of the surfaces involving SiX_2 species on them to gain insights into thermally activated etching processes in which the dihalide species are among the main products. One is a 3×1 surface consisting of alternating SiX_2 monomers and SiX dimers, and the other is a 2×1 surface with a lower coverage of the adsorbates than the 3×1 surface so that it is free from structural strain induced by the interadsorbate repulsions even if the adsorbates are large atoms such as Br and I. By examining the desorption energies of the SiX_2 units from both types of the surfaces and the total overlap populations with respect to the bonding between the units and the substrate, it has been revealed that the desorption energies can be affected by the presence of the adsorbates mainly through the following two factors: (1) the weakening of the backbonds through reduction in their bond charges induced by the adsorbates, and (2) the interatomic repulsion between the adsorbates. The factor (1) becomes significant in case the adsorbates are

electronegative elements such as Cl and Br. The factor (2) manifests itself when the adsorbates are large-sized elements and/or their coverage is high. The available experimental data on thermal desorption from the X/Si(100) surfaces has been interpreted consistently by taking account of both factors. A strong correlation between the total overlap populations (associated with the bonding between the SiX_2 and the surface) and the desorption energies of SiX_2 has been found, which suggests that the present population analysis scheme can serve as an interpretational tool for desorption energies obtained by total energy calculations that is expected to provide insights into, e.g., photo-induced etching processes.

Appendix A

A review of the development of the DFT-LDA approach to surfaces

In this appendix we give a brief review of the development of DFT-LDA calculations for surfaces. The application of the DFT-LDA scheme to solid surfaces began with work by Lang and Kohn [102, 103, 104]. In this work, the semi-infinite array of nuclei (or ions) composing the surface was replaced by a uniform (jellium) background to make calculations tractable. By dealing with such an extended surface rather than a cluster the role of the *sp* electrons of metals, which are expected to be rather delocalized, could be studied. This approach was applied to clean surfaces [102, 103] as well as surfaces with adsorbates [104], where the adsorbate layer was also replaced by a uniform background with its charge density different from that for the surface. In order to incorporate effects of the presence of a discrete lattice, they adopted a perturbation treatment [105]. For quantitative discussions, however, a nonperturbative treatment, i.e., taking full account of the lattice potential, was obviously needed.

Pioneering work along these lines was done by two groups, Appelbaum et al. for Na(100) [41], and Alldredge et al. for Li(100) [106, 42]. The approaches taken by these groups are common in that: (1) the wavefunctions

are expanded with a basis set consisting of two-dimensional plane waves to account for the translational symmetry in the direction parallel to the surface, and (2) the nuclei and core electrons of each atom were replaced by a pseudopotential representing the electron-ion interaction. Appelbaum et al. took the surface to be semi-infinite in the direction perpendicular to the surface. They obtained the wavefunctions by numerical integrations in the surface normal direction in the region of the vacuum and a few surface layers, after which they were matched to wavefunctions with bulk behavior. Alldredge et al., on the other hand, approximated the surface with a slab with finite thickness. In order to make the system periodic in all the three directions, the slab with a vacuum region was periodically repeated, where the vacuum region was taken to be sufficiently large to avoid the artificial interaction between neighboring slabs. They then expanded the wavefunctions in terms of sine and cosine functions (multiplied by two-dimensional plane waves) that are constrained to be zero in the mid-point of the vacuum region between neighboring slabs. However, this constraint is physically unnecessary, because the wavefunctions would have to decay in the vacuum region even without this requirement. Without this requirement, calculations can be made completely equivalent to bulk calculations in that wavefunctions can be expanded in terms of three-dimensional plane waves. In calculations by Schlüter et al. for Si(111) 1×1 and 2×1 surfaces [43, 44], a set of three-dimensional plane waves was used as a basis set to expand wavefunctions. The energy cutoff of the plane waves was 2.7 Ry, and additional plane waves up to an energy cutoff of 6 Ry were included in a perturbative way. The use of periodically placed slabs, pseudopotentials and a (three-dimensional) plane wave basis set has now become one of the most common way of studying electronic structures of both clean and adsorbate-covered surfaces.

Most DFT-LDA calculations in the 1970's, including the work mentioned above, focused on electronic structures and not on structural properties such as the equilibrium structures and phonon frequencies. However, accurate calculations of such structural properties would have been quite valuable, especially for studies of solid surfaces, due to the fact that surfaces often ex-

hibit complicated reconstructions and that elucidating surface structures has been one of the most active fields of surface science. The capability of DFT-LDA calculations to accurately reproduce and predict structural properties that has been well documented is largely indebted to the development of *ab initio* pseudopotentials. They are generated based only upon *ab initio* atomic calculations and do not rely on any experimental data. Before the advent of *ab initio* pseudopotentials, empirical pseudopotentials that were determined so as to fit experimental spectra for atoms or bulk solids had been made use of [107], and it was known that they did not work well in calculating structural properties. For instance, Wendel et al. calculated the total energy of crystalline Si as a function of the atomic displacements with the DFT-LDA scheme and found that the calculated equilibrium lattice constant was 4.7 Å, which is too short compared to the experimental value of 5.43 Å [108]. They attributed the discrepancy to the empirical pseudopotential they used. Harris et al. [109] and Zunger et al. [110, 111] developed schemes of generating nonempirical pseudopotentials from *ab initio* atomic calculations. With such pseudopotentials, structural properties of crystalline Si were shown to be reproduced much better than with empirical ones [112, 113].

Hamann, Schlüter and Chiang (HSC) then came up with *ab initio* norm-conserving pseudopotentials [32]. The norm-conservation requirement leads to a significantly improved *transferability* of the pseudopotentials among a variety of chemical environments, as described in Subsec. 2.1.2. In calculations by Yin and Cohen for crystalline Si with the HSC pseudopotential, the solid-solid phase transformation and lattice dynamics (i.e. phonon frequencies) as well as static structural properties were reproduced in good agreement with experiments [27, 114, 115]. They also applied the same calculational technique to clean Si(100) 2×1 surfaces, for which geometrical optimizations were performed by calculating the Hellmann-Feynman forces acted upon each atom in the system and a structure consisting of buckled dimers was determined to be the most stable structure [116]. The success of these calculations definitely showed that DFT-LDA first-principles calculations with *ab initio* norm-conserving pseudopotentials had become a very powerful tool in pre-

dicting various properties of bulk solids as well as surfaces.

With the progress of massively parallel computers and efficient computational schemes [28, 29, 6], DFT-LDA calculations are now capable of dealing with surfaces with large unit cells. For the Si(111) 7×7 reconstructed surface, for instance, the equilibrium structure [117, 118] as well as phonon spectra [119] were obtained in good agreement with experiments. Ab initio molecular dynamics simulations, in which the forces exerted upon the atoms are calculated from first principles in contrast to classical molecular dynamics simulations, have also been made possible. With this approach, De Vita et al. studied dissociative adsorption processes of Cl_2 molecules incident upon the Si(111) 2×1 surface [120, 121, 122].

References

- [1] P. Hohenberg and W. Kohn, Phys. Rev. **136**, B864 (1964).
- [2] For a general review, see, e.g., W. Kohn and P. Vashishta, in *Theory of the Inhomogeneous Electron Gas*, edited by S. Lundqvist and N.H. March (Plenum, New York, 1983) Chap. 2.
- [3] W. Kohn and L.J. Sham, Phys. Rev. **140**, A1133 (1965).
- [4] R.S. Mulliken, J. Chem. Phys. **23**, 1833; **23**, 2343 (1955).
- [5] R. Hoffmann, Rev. Mod. Phys. **60**, 601 (1988) ; J. Phys. Condens. Matter **5**, A1 (1993).
- [6] See, e.g., M.C. Payne, M.P. Teter, D.C. Allan, T.A. Arias and J.D. Joannopoulos, Rev. Mod. Phys. **64**, 1045 (1992).
- [7] N.W. Ashcroft and N.D. Mermin, *Solid State Physics* (Saunders College, 1976) Chapter 11.
- [8] H. Aizawa and S. Tsuneyuki, "First-Principles study of CO bonding to Pt(111): validity of the Blyholder model", to be published in Surf. Sci. Lett.
- [9] G. Blyholder, J. Phys. Chem. **68**, 2772 (1964).
- [10] S. Ishi, Y. Ohno and B. Viswanathan, Surf. Sci. **161**, 349 (1985).

- [11] A. Nilsson, N. Wassdahl, M. Weinelt, O. Karis, T. Wiell, P. Bennich, J. Hasselström, A. Föhlisch, J. Stöhr, and M. Samant, *Appl. Phys. A* **65**, 147 (1997).
- [12] A. Nilsson, M. Weinelt, T. Wiell, P. Bennich, O. Karis, N. Wassdahl, J. Stöhr, and M. Samant, *Phys. Rev. Lett.* **78**, 2847 (1997).
- [13] Y.-T. Wong and R. Hoffmann, *J. Phys. Chem.* **95**, 859 (1991).
- [14] P. Hu, D.A. King, M.-H. Lee and M.C. Payne, *Chem. Phys. Lett.* **246**, 73 (1995).
- [15] R.B. Jackman, H. Ebert and J.S. Foord, *Surf. Sci.* **176**, 183 (1986).
- [16] Q. Gao, C.C. Cheng, P.J. Chen, W.J. Choyke, and J.T. Yates, Jr., *J. Chem. Phys.* **98**, 8308 (1993).
- [17] A. Szabó, P.D. Farrall and T. Engel, *Surf. Sci.* **312**, 284 (1994).
- [18] R.B. Jackman, R.J. Price and J.S. Foord, *App. Surf. Sci.* **36**, 296 (1989).
- [19] M.C. Flowers, N.B.H. Jonathan, Y. Liu and A. Morris, *Surf. Sci.* **343**, 133 (1995).
- [20] S.M. Gates, R.R. Kunz and C.M. Greenlief, *Surf. Sci.* **207**, 364 (1989).
- [21] C.C. Cheng and J.T. Yates, Jr., *Phys. Rev. B* **43**, 4041 (1991).
- [22] See, e.g., P. Fulde, *Electron Correlations in Molecules and Solids*, 2nd edition (Springer-Verlag, Berlin, 1993).
- [23] See, e.g., I. Shavitt, in *Modern Theoretical Chemistry*, Vol. 3, edited by H.F. Schaefer, (Plenum, New York, 1977), p.189.
- [24] L. Hedin, *Phys. Rev.* **139**, A796 (1965).

- [25] L. Hedin and S. Lundqvist, *Solid State Physics Vol. 23*, edited by F. Seitz, D. Tuenbull and H. Ehrenreich (Academic, New York, 1969) p. 1.
- [26] M.S. Hybertsen and S.G. Louie, *Phys. Rev. B* **34**, 5390 (1986).
- [27] M.T. Yin and M.L. Cohen, *Phys. Rev. Lett.* **45**, 1004 (1980).
- [28] R. Car and M. Parrinello, *Phys. Rev. Lett.* **55**, 2471 (1985).
- [29] M.P. Teter, M.C. Payne and D.C. Allan, *Phys. Rev. B* **40**, 12255 (1989).
- [30] L. Kleinman and D.M. Bylander, *Phys. Rev. Lett.* **48**, 1425 (1982).
- [31] N. Troullier and J.L. Martins, *Phys. Rev. B* **43**, 1993 (1991).
- [32] D.R. Hamann, M. Schlüter and C. Chiang, *Phys. Rev. Lett.* **43**, 1494 (1979).
- [33] G.B. Bachelet, D.R. Hamann, and M. Schlüter, *Phys. Rev. B* **26**, 4199 (1982).
- [34] D. Vanderbilt, *Phys. Rev. B* **41**, 7892 (1990).
- [35] See, e.g., S.R. Morrison, *The Chemical Physics of Surfaces*, 2nd edition (Plenum, New York, 1990), Sec. 5.2.
- [36] G. te Velde and E.J. Baerends, *Chem. Phys.* **177**, 399 (1993).
- [37] K. Hermann, P.S. Bagus and C.J. Nelin, *Phys. Rev. B* **35**, 9467 (1987).
- [38] H. Aizawa and S. Tsuneyuki, *Surf. Sci.* **363**, 223 (1996).
- [39] H. Aizawa and S. Tsuneyuki, in *Elementary Processes in Excitations and Reactions on Solid Surfaces*, edited by A. Okiji, H. Kasai and K. Makoshi (Springer-Verlag, Berlin, 1996), p. 45.
- [40] S.-S. Sung and R. Hoffmann, *J. Am. Chem. Soc.* **107**, 578 (1985).

- [41] J.A. Appelbaum and D.R. Hamann, Phys. Rev. B **6**, 2166 (1972).
- [42] G.P. Alldredge and L. Kleinman, Phys. Rev. B **10**, 559 (1974).
- [43] M. Schlüter, J.R. Chelikowsky, S.G. Louie and M.L. Cohen, Phys. Rev. Lett. **34**, 1385 (1975).
- [44] M. Schlüter, J.R. Chelikowsky, S.G. Louie and M.L. Cohen, Phys. Rev. B **12**, 4201 (1975).
- [45] J.R. Chelikowsky, M. Schlüter, S.G. Louie and M.L. Cohen, Solid State Commun. **17**, 1103 (1975).
- [46] H. Chang, J.F. Harrison, T.A. Kaplan and S.D. Mahanti, Phys. Rev. B **49**, 15753 (1994).
- [47] C.W. Bauschlicher, Jr. and P.S. Bagus, J. Chem. Phys. **81**, 5889 (1984).
- [48] P.S. Bagus, F. Illas, C. Sousa and G. Pacchioni, in *Electronic Properties of Solids Using Cluster Methods*, edited by T.A. Kaplan and S.D. Mahanti (Plenum, New York, 1995) p. 93.
- [49] C.J. Nelin, P.S. Bagus and M.R. Philpott, J. Chem. Phys. **87**, 2170 (1987).
- [50] P.S. Bagus, G. Pacchioni and M.R. Philpott, J. Chem. Phys. **90**, 4287 (1989).
- [51] P.S. Bagus and F. Illas, Phys. Rev. B **42**, 10852 (1990).
- [52] I.P. Batra and P.S. Bagus, J. Vac. Sci. Technol. A **6**, 600 (1988).
- [53] B. Hammer, Y. Morikawa and J.K. Nørskov, Phys. Rev. Lett. **76** 2141 (1996).
- [54] Y. Morikawa, J.J. Mortensen, B. Hammer and J.K. Nørskov, Surf. Sci. **386**, 67 (1997).

- [55] R.J. Smith, J. Anderson and G.J. Lapeyre, Phys. Rev. B **22**, 632 (1980).
- [56] C.F. McConville, C. Somerton and D.P. Woodruff, Surf. Sci. **139**, 75 (1984).
- [57] R. Miranda, K. Wandelt, D. Rieger and R.D. Schnell, Surf. Sci. **139**, 430 (1984).
- [58] G. Rangelov, N. Memmel, E. Bertel and V. Dose, Surf. Sci. **251/252**, 965 (1991).
- [59] G. Ertl, M. Neumann and K.M. Streit, Surf. Sci. **64**, 393 (1977).
- [60] H. Froitzheim, H. Hopster, H. Ibach and S. Lehwald, Appl. Phys. **13**, 147 (1977).
- [61] B.E. Hayden and A.M. Bradshaw, Surf. Sci. **125**, 787 (1983).
- [62] P.R. Norton, J.W. Goodale and E.B. Selkirk, Surf. Sci. **83**, 189 (1979).
- [63] V. Dose, Surf. Sci. Rep. **5**, 337 (1985).
- [64] K. Fukutani, M.-B. Song and Y. Murata, J. Chem. Phys. **103**, 2221 (1995).
- [65] K. Fukutani, T.T. Magkoev, Y. Murata and K. Terakura, Surf. Sci. **363**, 185 (1996).
- [66] H. Nakatsuji, H. Morita, H. Nakai, Y. Murata and K. Fukutani, J. Chem. Phys. **104**, 714 (1996).
- [67] D.W. Turner, C. Baker, A.D. Baker and C.R. Brundle, *Molecular Photoelectron Spectroscopy* (Wiley, London, 1970).
- [68] K.P. Huber and G. Herzberg, *Molecular Spectra and Molecular Structure IV. Constants of Diatomic Molecules* (Van Nostrand Reinhold, New York, 1979).

- [69] P. Skytt, P. Glans, K. Gunnelin, J. Guo, J. Nordgren, Y. Luo and H. Ågren, *Phys. Rev. A* **55**, 134 (1997).
- [70] H.F. Winters and J.W. Coburn, *Surf. Sci. Rep.* **14**, 161 (1992).
- [71] J.W. Coburn, *Appl. Phys. A* **59**, 451 (1994).
- [72] K. Shudo, F. Komori, K. Hattori and Y. Murata, *Surf. Sci.* **320**, 161 (1994).
- [73] F. Komori, K. Shudo, K. Hattori, T. Iimori and Y. Murata, *Surf. Sci.* **363**, 268 (1996).
- [74] K. Hattori, K. Shudo, T. Iimori, F. Komori and Y. Murata, *J. Phys.: Condens. Matter* **8**, 6543 (1996).
- [75] T.N. Rhodin and C. Paulsen-Boaz, *Surf. Sci.* **363**, 240 (1996).
- [76] J.J. Boland, *Phys. Rev. Lett.* **65**, 3325 (1990).
- [77] J.J. Boland, *Surf. Sci.* **261**, 17 (1992).
- [78] Y.J. Chabal and K. Raghavachari, *Phys. Rev. Lett.* **54**, 1055 (1985).
- [79] T. Sakurai and H.D. Hagstrum, *Phys. Rev. B* **14**, 1593 (1976).
- [80] J.E. Northrup, *Phys. Rev. B* **44**, 1419 (1991).
- [81] J.E. Rowe, G. Margaritondo and S.B. Christman, *Phys. Rev. B* **16**, 1581 (1977).
- [82] G. Thornton, P.L. Wincott, R.M. Grath, I.T. McGovern, F.M. Quinn, D. Norman and D.D. Vvedensky, *Surf. Sci.* **211/212**, 959 (1989).
- [83] C.C. Cheng, Q. Gao, W.J. Choyke, and J.T. Yates, Jr., *Phys. Rev. B* **46**, 12810 (1992).
- [84] J.J. Boland, *Science* **262**, 1703 (1993).

- [85] P. Krüger and J. Pollmann, *Phys. Rev. B* **47**, 1898 (1993).
- [86] G.S. Khoo and C.K. Ong, *Phys. Rev. B* **52**, 2574 (1995).
- [87] G.A. de Wijs and A. Selloni, *Phys. Rev. Lett.* **77**, 881 (1996).
- [88] V. Eteläniemi, E.G. Michel and G. Materlik, *Surf. Sci.* **251/252**, 483 (1991).
- [89] D. Rioux, M. Chander, Y.Z. Li and J.H. Weaver, *Phys. Rev. B* **49**, 11071 (1994).
- [90] J. Lohmüller, H.H. Bertschat, H. Granzer, H. Haas, G. Schatz, W.-D. Zeitz and ISOLDE Collaboration, *Surf. Sci.* **360**, 213 (1996).
- [91] D. Rioux, F. Stepniak, R.J. Pechman and J.H. Weaver, *Phys. Rev. B* **51**, 10981 (1995).
- [92] P.-L. Cao and R.-H. Zhou, *J. Phys.: Condens. Matter* **5**, 2897 (1993).
- [93] A. Szabó and T. Engel, *J. Vac. Sci. Technol. A* **12**, 648 (1994).
- [94] N. Materer, R.S. Goodman and S.R. Leone, *J. Vac. Sci. Technol. A* **15**, 2134 (1997).
- [95] M. Chander, Y.Z. Li, D. Rioux and J.H. Weaver, *Phys. Rev. Lett.* **71**, 4154 (1993).
- [96] G.A. de Wijs, A. De Vita and A. Selloni, *Phys. Rev. Lett.* **78**, 4877 (1997).
- [97] Y.J. Chabal and K. Raghavachari, *Phys. Rev. Lett.* **53**, 282 (1984).
- [98] CRC Handbook of Chemistry and Physics, 77th edition (Chemical Rubber, Cleveland, 1996).
- [99] A.D. Corso, A. Pasquarello, A. Baldereschi and R. Car, *Phys. Rev. B* **53**, 1180 (1996).

- [100] L. Pauling, *The Chemical Bond*, Cornell University Press (1967).
- [101] D.J. Chadi, Phys. Rev. Lett. **41**, 1062 (1978).
- [102] N.D. Lang, Solid State Commun. **7**, 1047 (1969).
- [103] N.D. Lang and W. Kohn, Phys. Rev. B **1**, 4555 (1970).
- [104] N.D. Lang, Phys. Rev. B **4**, 4234 (1971).
- [105] N.D. Lang and W. Kohn, Phys. Rev. B **3**, 1215 (1971).
- [106] G.P. Alldredge and L. Kleinman, Phys. Rev. Lett. **28**, 1264 (1972).
- [107] See, e.g., Solid State Physics Vol. 24, edited by H. Ehrenreich, F. Seitz and D. Tuenbull (Academic, New York, 1970).
- [108] H. Wendel and R.M. Martin, Phys. Rev. Lett. **40**, 951 (1978).
- [109] J. Harris and R.O. Jones, Phys. Rev. Lett. **41**, 191 (1978).
- [110] A. Zunger and M.L. Cohen, Phys. Rev. Lett. **41**, 53 (1978).
- [111] A. Zunger and M.L. Cohen, Phys. Rev. B **18**, 5449 (1978).
- [112] J.A. Vergés and C. Tejedor, Phys. Rev. B **20**, 4251 (1979).
- [113] A. Zunger, Phys. Rev. B **21**, 4785 (1980).
- [114] M.T. Yin and M.L. Cohen, Phys. Rev. B **26**, 3259 (1982).
- [115] M.T. Yin and M.L. Cohen, Phys. Rev. B **26**, 5668 (1982).
- [116] M.T. Yin and M.L. Cohen, Phys. Rev. B **24**, 2303 (1981).
- [117] I. Štich, M.C. Payne, R.D. King-Smith, J.-S. Lin and L.J. Clarke, Phys. Rev. Lett. **68**, 1351 (1992).
- [118] K.D. Brommer, M. Needels, B.E. Larson and J.D. Joannopoulos, Phys. Rev. Lett. **68**, 1355 (1992).

- [119] I. Štich, K. Terakura and B.E. Larson, Phys. Rev. Lett. **74**, 4491 (1995).
- [120] A. De Vita, I. Štich, M.J. Gillan, M.C. Payne and L.J. Clarke, Phys. Rev. Lett. **71**, 1276 (1993).
- [121] I. Štich, M.C. Payne, A. De Vita, M.J. Gillan and L.J. Clarke, Chem. Phys. Lett. **212**, 617 (1993).
- [122] I. Štich, A. De Vita, M.C. Payne, M.J. Gillan and L.J. Clarke, Phys. Rev. B **49**, 8076 (1994).

